

Effects of shape coexistence and configuration mixing on low-lying states in tellurium isotopes

Kosuke Nomura^{1, 2, *}

¹*Department of Physics, Hokkaido University, Sapporo 060-0810, Japan*

²*Nuclear Reaction Data Center, Hokkaido University, Sapporo 060-0810, Japan*

(Dated: March 11, 2026)

Low-energy quadrupole collective states in even-even tellurium (Te) isotopes are studied using the interacting boson model with configuration mixing. The corresponding Hamiltonian is determined by means of the microscopic nuclear structure calculations within the self-consistent mean-field method employing a given energy density functional and pairing interaction. Calculated low-energy levels for nonyrast states show a parabolic behavior characteristic of the shape-coexisting structure. The intruder prolate-shape configuration is shown to mix strongly with the normal oblate-shape configuration, and play an important role in determining the low-lying structure in the Te isotopes near the middle of the neutron major shell closures.

I. INTRODUCTION

Low-energy structure of nuclei near the proton major shell closure $Z = 50$ has been considered a textbook example exhibiting a vibrational energy spectrum of multiphonon excitations. However, in light of recent experimental studies producing new spectroscopic data, this interpretation does not necessarily apply to many of those nuclei in this mass region. For cadmium (Cd) isotopes in the middle of the neutron major shells $N = 50$ and 82 , for instance, some low-spin states were observed at excitation energies close to those of the two- or three-phonon multiplets; these states cannot be explained in terms of a pure vibrational picture. These additional low-energy states in the Cd isotopes have been attributed to contributions of intruder excitations across the proton $Z = 50$ major shell [1–6]. A similar mechanism is expected to be at work in tin (Sn) isotopes.

Noticeable effects of the cross-shell intruder excitations are the parabolic behaviors of bands built on the low-lying excited 0^+ states. These features are most spectacularly seen in neutron-deficient lead (Pb) and mercury (Hg) nuclei, which are close to the proton $Z = 82$ major shell. The appearance of the low-energy intruder 0^+ band has been interpreted as a signature of coexistence of intrinsic shapes [3, 4, 6–8]. In ^{186}Pb , for instance, the ground-state band has been empirically associated with a spherical shape, and the low-energy 0_2^+ and 0_3^+ excited bands were attributed to be a weakly oblate-deformed and a strongly prolate-deformed shapes [9]; updated experimental data for this nucleus suggested that the 0_2^+ and 0_3^+ bands were associated with the prolate and oblate configurations, respectively [10]. In the mean-field approximation [4, 6, 9, 11–13], coexistence of multiple shapes in the vicinity of the ground state is inferred from the presence of several local minima in the potential energy surface (PES) in terms of relevant collective coordinates. The shape coexistence has been observed in

a wide range of the nuclear chart, and is nowadays regarded as a universal phenomenon in nuclear many-body systems.

Here the low-energy structure of even-even tellurium (Te) isotopes is of special interest. Since they are also close to the proton $Z = 50$ major shell, similar cross-shell excitations to those in the Cd and Sn isotopic chains are expected to take place and play relevant roles at low energy. The effect of shape coexistence in the mass region below the $Z = 50$ major shell, including the midshell Cd and Sn isotopes and those zirconium and molybdenum nuclei near $N = 60$, has been extensively studied experimentally, and by related theoretical approaches (see recent reviews [7, 8] and references therein). Most recent studies on nuclei near $Z = 50$ include ones that showed appearance of multiple shape coexistence in $^{110,112}\text{Cd}$ [14, 15] from comparisons to beyond-mean-field calculations, and those for the neighboring Sn isotopes in the neutron midshell [16–18], which suggested possible configuration mixing in these isotopes on the basis of the phenomenological interacting boson model (IBM) calculations. Concerning the Te isotopes, earlier experimental study [19] suggested intruder states in those nuclei near the middle of the neutron major shells. Low-energy levels in ^{116}Te [20] and ^{118}Te [21] were measured in more recent studies, in which the emergence of shape coexistence was discussed. Lifetime measurements were carried out to extract the systematic of the excitation energies and $B(E2)$ values for low-lying states [22–24]. Related theoretical calculations that were previously reported include those within the nuclear shell model [23, 25–27], static [28, 29] and beyond [30–34] mean-field methods, the IBM [19–21, 35–38], the geometrical collective model [39] and effective field theory [40]. The interpretation of the nuclear structure in Te nuclei in terms of the shape coexistence does not appear to have been established as firmly as for those nuclei below $Z = 50$. Further theoretical investigations would help identifying regions of shape coexistence in the neutron-deficient $Z > 50$ nuclei.

In the present work, roles played by the intruder configurations in the low-lying structure of midneutron-shell

* nomura@sci.hokudai.ac.jp

Te isotopes are investigated by using the IBM in its appropriate version that incorporates configuration mixing of the normal and intruder states. This version of the IBM was previously applied to identify possible intruder states in Cd (e.g., [3, 5, 35, 36, 41–51]), Sn (e.g., [16–18]), and Te (e.g., [3, 19–21, 35–37]) nuclei. In most of these studies, the IBM calculations were performed either with model parameters being fitted to observed low-energy spectroscopic properties or assuming dynamical symmetries for normal and intruder configurations. In Ref. [43], a microscopic derivation of the IBM parameters for the normal configuration of Cd nuclei was also made using the Otsuka-Arima-Iachello mapping procedure [52]. The present study is based on the microscopic framework of the nuclear energy density functional (EDF): the self-consistent mean-field (SCMF) calculations employing a given EDF provide microscopic inputs to determine the parameters of the IBM Hamiltonian that incorporates the configuration mixing [53, 54]. This method was previously employed for systematic studies on the shape evolution and coexistence, and related spectroscopic properties in different mass regions: neutron-deficient Pb [53] and Hg [55], mid-neutron-shell Cd [49], and neutron-rich Sr, Zr, Mo, and Ru nuclei near $N = 60$ [56], neutron-deficient and neutron-rich Ge, Se [57], and Kr [58] isotopes.

For the microscopic part of the theoretical analysis, the SCMF calculations are performed within the framework of the relativistic Hartree-Bogoliubov (RHB) model [59–62]. The RHB framework was actually adopted in recent studies [28, 34] in order to analyze shape evolution and coexistence in the Te isotopes. The RHB self-consistent calculations in these studies produced the PESs, which exhibit a prolate-to-oblate shape transition and coexistence in the midshell Te nuclei. In Ref. [34], in particular, spectroscopic properties of the Te nuclei were computed in terms of the quadrupole collective Hamiltonian (QCH), with the deformation-dependent mass parameters and moments of inertia determined by the RHB-SCMF solutions. The present work employs the same microscopic inputs from the RHB-SCMF calculations as those for the QCH considered in the previous study [34], and hence gives an alternative description of the spectroscopic properties of Te isotopes using the EDF-mapped IBM.

In the following, the theoretical method is described in Sec. II. The calculated results for the PESs, low-energy spectra, and electromagnetic transition properties for the even-even $^{108-126}\text{Te}$ are presented in Sec. III. Some dependence of the calculated results on the EDF is also discussed in the same section. Section IV gives a summary and conclusions.

II. THEORETICAL FRAMEWORK

The first step is a set of constrained RHB-SCMF calculations for each nucleus, with the constraints being on

the mass quadrupole moments that are related to the intrinsic axially symmetric deformation β and triaxiality γ [63], respectively. The constrained calculations provide PESs in terms of the (β, γ) deformations. The underlying interaction is the density-dependent point-coupling (DD-PC1) EDF [64] for the particle-hole part. The DD-PC1 set is a representative class of the relativistic EDF, and has been successfully used for numerous nuclear structure studies. For the particle-particle part, a separable pairing force of finite range of Ref. [65] is adopted, with the standard value of the pairing strength, 728 MeV fm^3 , throughout the present study. Further details of the RHB calculations are found in Ref. [34].

The second step is to construct the boson Hamiltonian. Here the neutron-proton version of the IBM (referred to as IBM-2) is employed, in which neutron and proton degrees of freedom are distinguished. Accordingly, the IBM-2 with configuration mixing is hereafter denoted IBM2-CM. The building blocks of the IBM-2 are neutron monopole s_ν and quadrupole d_ν bosons, and proton monopole s_π and quadrupole d_π bosons. The neutron (proton) s_ν and d_ν (s_π and d_π) bosons reflect, from a microscopic point of view [52, 66], collective monopole and quadrupole pairs of valence neutrons (protons), respectively. The number of neutron (proton) bosons, denoted N_ν (N_π), is equal to the number of neutron (proton) pairs counted from the nearest closed shell, and is conserved for a given nucleus. In the present case, $N_\pi = 1$ and $N_\nu = 3 - 8$ for $^{108-118}\text{Te}$, respectively, and $N_\nu = 7 - 4$ for $^{120-126}\text{Te}$, respectively.

The intruder configurations here represent the $2n$ -particle- $2n$ -hole ($n = 1, 2, \dots$) excitations of protons across the $Z = 50$ shell and are described by the unperturbed IBM-2 Hamiltonians for $(N_\nu, N_\pi + 2n)$ bosons [67]. As is usual in previous IBM2-CM studies, like-particle bosons are not distinguished from like-hole bosons. In the present work, two-boson configurations; that is, normal (0p-0h) and intruder (2p-2h), are considered. This is based on the fact that, as shown below, the RHB-SCMF calculation suggests basically two (oblate global and prolate local) minima in the PESs for the midshell Te nuclei. The IBM2-CM space is defined as a direct sum of the two unperturbed IBM-2 spaces consisting of (N_ν, N_π) and $(N_\nu, N_\pi + 2)$ bosons, and is expressed as

$$[N_\nu \otimes N_\pi] \oplus [N_\nu \otimes (N_\pi + 2)]. \quad (1)$$

The corresponding IBM2-CM Hamiltonian is written as

$$\hat{H} = \hat{P}_1 \hat{H}_1 \hat{P}_1 + \hat{P}_3 (\hat{H}_3 + \Delta) \hat{P}_3 + \hat{V}_{\text{mix}}, \quad (2)$$

where \hat{H}_1 and \hat{H}_3 denote the Hamiltonians for the unperturbed spaces of $N_\pi = 1$ and three bosons, \hat{P}_1 and \hat{P}_3 are operators projecting onto each unperturbed space, Δ denotes the energy required for the 2p-2h excitation, and the last term stands for the interaction that mixes the two IBM-2 spaces. For the unperturbed IBM-2 Hamiltonian for the normal ($i = 1$) or intruder ($i = 3$) configuration the following simplified form is adopted:

$$\hat{H}_i = \epsilon_{d,i} (\hat{n}_{d_\nu} + \hat{n}_{d_\pi}) + \kappa_i \hat{Q}_{\nu,i} \cdot \hat{Q}_{\pi,i}, \quad (3)$$

where in the first term $\hat{n}_{d_\rho} = d_\rho^\dagger \cdot \tilde{d}_\rho$ represents the neutron ($\rho = \nu$) or proton ($\rho = \pi$) d -boson number operator with the energy $\epsilon_{d,i}$ with respect to s_ρ bosons, and the second term represents the quadrupole-quadrupole interaction between neutron and proton bosons with strength κ_i . The quadrupole operator $\hat{Q}_{\rho,i} = s_\rho^\dagger \tilde{d}_\rho + d_\rho^\dagger \tilde{s}_\rho + \chi_{\rho,i} (d_\rho^\dagger \times \tilde{d}_\rho)^{(2)}$ with $\chi_{\rho,i}$ being a dimensionless parameter. The mixing term reads

$$\hat{V}_{\text{mix}} = \omega (s_\pi^\dagger \cdot s_\pi^\dagger + d_\pi^\dagger \cdot d_\pi^\dagger) + (H.c.), \quad (4)$$

with the strength ω assumed to be equal for the s_π and d_π boson terms. Note that the forms (3) and (4) are the same as those used in the previous IBM2-CM studies for the Hg isotopes [55], except that the rotational term $\hat{L} \cdot \hat{L}$ and the three-body boson terms are not included in the present work. More details about the Hamiltonian are found in [55].

The IBM2-CM Hamiltonian is determined by associating it with the corresponding SCMF PES [53]. The geometry of the IBM2-CM Hamiltonian is realized as a 2×2 matrix

$$\mathcal{E}(\beta, \gamma) = \begin{pmatrix} E_{11}(\beta, \gamma) & \Omega_{13}(\beta, \gamma) \\ \Omega_{31}(\beta, \gamma) & E_{33}(\beta, \gamma) \end{pmatrix}, \quad (5)$$

calculated as the expectation value of the Hamiltonian (2) in the boson coherent state expressed as a direct sum of those for the two independent boson spaces [68]. The diagonal elements E_{ii} in (5) are expectation values of the unperturbed Hamiltonians, while the nondiagonal parts $\Omega_{13} = \Omega_{31}$ are those of the mixing term (4). As is conventional, the lower-energy eigenvalue of the coherent-state matrix (5) is taken as the IBM2-CM energy surface. Explicit analytic forms of E_{ii} and Ω_{13} are found in Ref. [55].

The parameters for the unperturbed Hamiltonian \hat{H}_1 are fixed [69] so that the expectation value of the unperturbed Hamiltonian, that is, the diagonal element of the coherent-state matrix E_{11} , should reproduce basic features of the RHB-SCMF PES in the vicinity of the oblate global minimum, with the corresponding β deformation denoted β_{gl} . The Hamiltonian for the intruder configuration \hat{H}_3 is determined in a similar way, i.e., by associating E_{33} to the local prolate minimum in the RHB-SCMF PES with a larger β deformation denoted β_{lo} .

Having fixed the unperturbed Hamiltonian parameters, the offset energy Δ is extracted so that the energy difference between the global and local minima in the SCMF PES should be reproduced, that is, the relation

$$[E_{33}(\beta_{lo}, \gamma_{lo}) + \Delta] - E_{11}(\beta_{gl}, \gamma_{gl}) = \delta E \quad (6)$$

is made to hold. $E_{11}(\beta_{gl}, \gamma_{gl})$ and $E_{33}(\beta_{lo}, \gamma_{lo})$ denote the diagonal elements of the matrix (5) calculated at the configurations $(\beta_{gl}, \gamma_{gl})$ and $(\beta_{lo}, \gamma_{lo})$. δE is the energy at the prolate local minimum relative to that at the oblate global minimum in the SCMF PES. Finally, the mixing interaction \hat{V}_{mix} is introduced, and the coherent-state matrix (5) is diagonalized. The mixing strength ω

is determined so that the IBM2-CM PES, i.e., the lowest eigenvalue of the matrix, should reasonably reproduce the γ dependence of that part of the PES between the oblate and prolate minima.

A special treatment should be made of the offset energy Δ . This parameter was originally defined [70] as a constant added to the energy eigenvalue for the ground state $E_3(0_{gs}^+)$ of the unperturbed intruder Hamiltonian so that it should become higher than the ground-state energy eigenvalue $E_1(0_{gs}^+)$ of the unperturbed normal configuration by an amount $\delta E'$, which is approximately set equal to the observed 0_2^+ excitation energy:

$$E_3(0_{gs}^+) + \Delta = E_1(0_{gs}^+) + \delta E' . \quad (7)$$

In the previous mapped IBM2-CM study of the shape coexistence in Pb isotopes [53], instead of the Δ values determined by the formula (6), those Δ values obtained from the formula (7), but with $\delta E'$ replaced with δE , i.e.,

$$E_3(0_{gs}^+) + \Delta = E_1(0_{gs}^+) + \delta E \quad (8)$$

were used to compute spectroscopic properties. In other words, a different Δ value from that obtained from the PES-mapping procedure was employed when diagonalizing the Hamiltonian. The 0_{gs}^+ energy eigenvalue of the (unperturbed) boson Hamiltonian comprises the energies gained by deformations at the mean-field level, and quantum correlation energies that are beyond the mean-field level. While among those parameters involved in the IBM2-CM Hamiltonian the Δ parameter should be most relevant to account for the ground-state correlation effects, the Δ values in (6) are defined in terms only of the deformation energies at the mean-field level. Since the quantum correlation energies are included only through the diagonalization of the boson Hamiltonian in the laboratory frame, it appears to be more appropriate to employ the Δ values obtained by (8) for calculating spectroscopic properties than those from (6).

In fact, it was shown in [53] that the Δ values obtained from the formula (6) turned out to be considerably smaller than those from (8), and that the deformed intruder 0^+ state became the ground state, which contradicts the empirical finding. The reason for this was that for the Pb isotopes the normal configuration was associated with the spherical mean-field minimum and did not gain energies arising from deformations. In the present case, the Δ values from (6) are shown to be systematically larger than those from (8) approximately by 0.6 MeV. This is because the normal configuration gains substantial amounts of correlation energies through the diagonalization due to large quadrupole-quadrupole interaction. Once the configuration mixing is carried out, the resultant energy levels for nonyrast states are overall substantially higher than the experimental ones and, in particular, the observed orders of levels are not reproduced. Another notable consequence of using the Δ values from (6) is that the $E2$ transitions of the nonyrast states, particularly the 0_2^+ state, turn out to be negligibly

small. This was also encountered in previous applications of the IBM2-CM mapping (e.g., [49, 56]), in which the Δ values calculated by the formula (6) were used for spectroscopic calculations, and $E2$ transitions for nonyrast states in some nuclei were not properly reproduced.

The Δ values of (8), however, do not necessarily reproduce accurately the features of the SCMF PESs, in particular, the oblate-prolate energy balance, that is, difference in energy between the oblate and prolate minima. The uncertainty of the parameters for the IBM2-CM was also noticed in Ref. [68], in which the IBM2-CM parameters that gave a good reproduction of low-lying states in the ^{186}Pb nucleus were shown to produce only two mean-field minima in the energy surface after configuration mixing. This is in contrast with the empirical understandings [9, 10] that the structure of ^{186}Pb is characterized by the coexistence of the spherical, oblate, and prolate shapes. It seems to be an open question to develop a consistent way of deriving Δ values that simultaneously give reasonable descriptions of the PESs and spectroscopic properties in the IBM2-CM mapping.

The IBM2-CM Hamiltonian with the parameters obtained by the aforementioned procedure is diagonalized in the space (1) using the boson m -scheme basis [53]. As noted, the IBM2-CM calculations are performed specifically for $^{114-122}\text{Te}$, for which the self-consistent calculations suggest two minima [34]. The standard EDF-mapped IBM-2 calculations, i.e., those that consist only of a single (normal) boson configuration and do not include the configuration mixing, are carried out for the other isotopes $^{108-112}\text{Te}$ and $^{124,126}\text{Te}$. In order to compare with the IBM2-CM results, the standard IBM-2 mapping calculations are also made for $^{114-122}\text{Te}$. Furthermore, the standard IBM-2 with a single configuration is below referred to as IBM-2, for the sake of simplicity.

III. RESULTS

A. Energy surfaces

Figures 1 and 2 show, respectively, the RHB-SCMF PESs and corresponding bosonic PESs for the nuclei $^{108-126}\text{Te}$. For obtaining the IBM2-CM PESs for $^{114-122}\text{Te}$ the Δ values of the formula (6) are used. The RHB-SCMF PESs suggest a transition from prolate to oblate shapes along the isotopic chain from near the neutron major shell $N = 50$ toward the other end, $N = 82$. There appears pronounced coexistence of the oblate global minimum in $\beta \approx 0.15 - 0.2$ and a prolate or triaxial minimum at $\beta \approx 0.3$ in transitional nuclei $^{114-120}\text{Te}$. The prolate local minimum is also visible in ^{122}Te , but is much more minor than in $^{114-120}\text{Te}$. More detailed discussions about the shape evolution inferred from the mean-field energy surfaces are found in Ref. [34]. One can see in Fig. 2 that basic properties and systematic of the mapped bosonic PESs, such as the location of the minima, softness in the β and γ deforma-

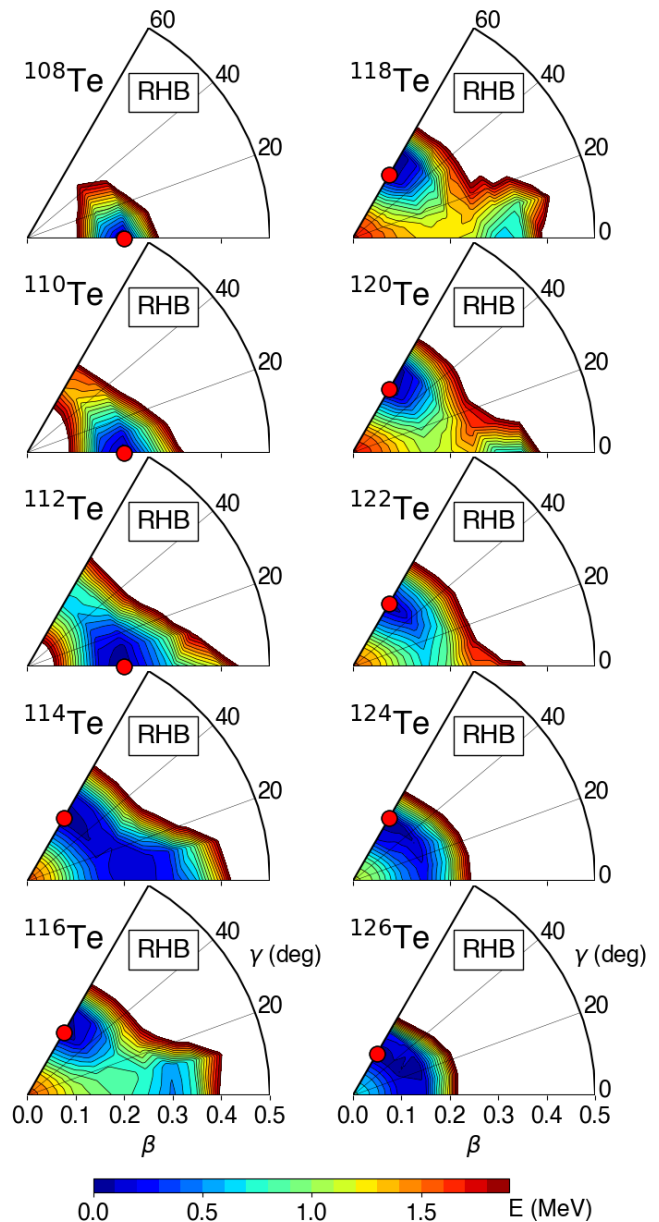


FIG. 1. Potential energy surfaces in terms of the quadrupole deformations β and γ for the $^{108-126}\text{Te}$ isotopes calculated by the constrained RHB-SCMF method employing the DD-PC1 EDF and a separable pairing force. The global minimum is indicated by the solid circle. See the main text for details.

tions, depth of the potential valley, etc., resemble those of the original RHB-SCMF PESs. A noticeable difference is that the bosonic PESs are rather flat as compared with the SCMF ones. The reason for this is that the IBM space is essentially comprised of valence nucleons only, while the SCMF model is generally built on an entire fermion model space consisting of a larger number of single-particle states.

In addition, in view of the recent finding that multiple

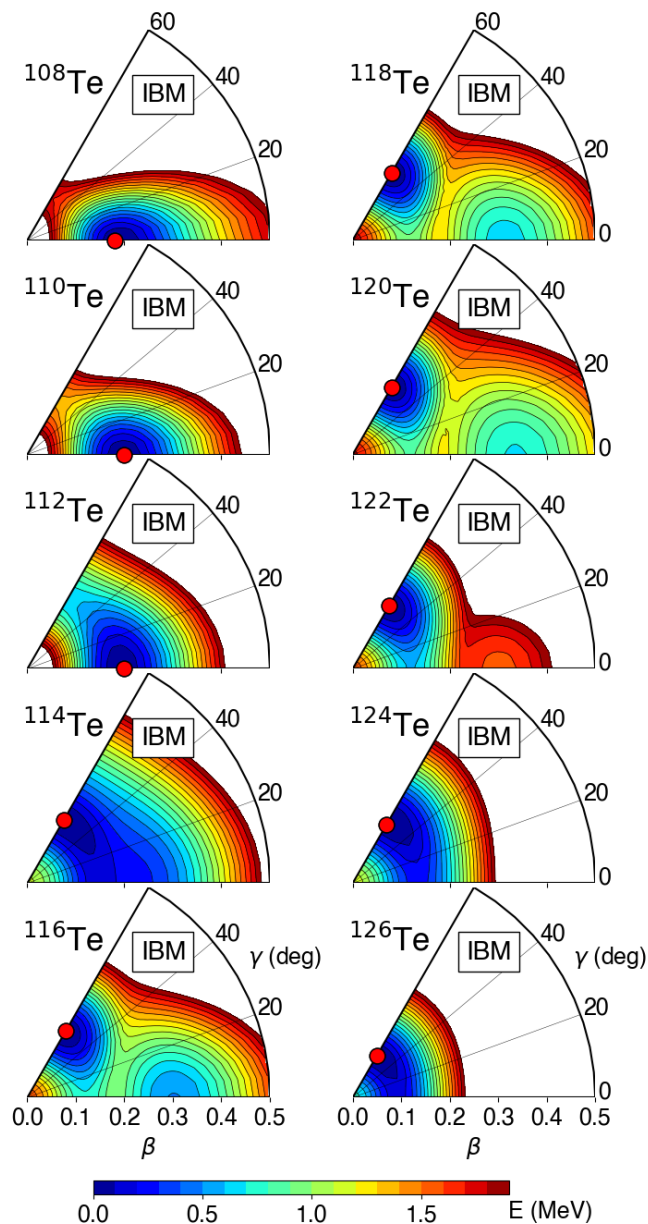


FIG. 2. Same as the caption to Fig. 1, but for the mapped bosonic PESs.

shapes emerge in midshell Cd isotopes [14], using two-boson configurations for the midshell Te isotopes may seem to be insufficient to fully take into account possible effects of mixing of shapes other than the oblate and prolate ones on the low-energy structure. For the SCMF-PES mapping procedure, however, especially if the potential is soft, such as in the case of ^{114}Te , constraining the parameters of more than two unperturbed IBM-2 Hamiltonians, energy offsets and mixing strengths would be practically difficult, and this is the reason why the present calculation is restricted to two-boson spaces. The prolate-oblate energy balance of the mean-field min-

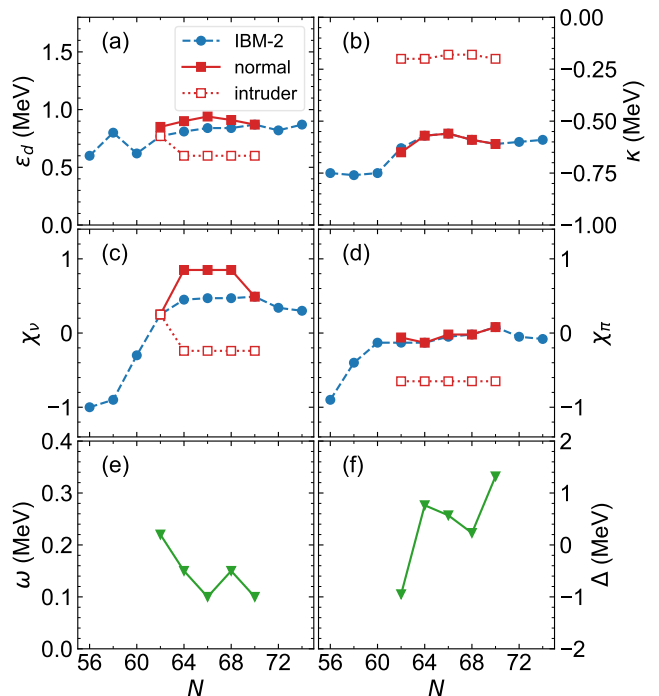


FIG. 3. Derived Hamiltonian parameters for the IBM-2 and those for the IBM2-CM corresponding to the normal and intruder configurations, mixing strength and energy offset Δ of (8) for the studied Te nuclei.

ima and γ softness are also rather sensitive to the EDFs used in the SCMF calculations. This point will be discussed in more detail in Sec. III D.

The parameters for the IBM2-CM Hamiltonian derived from the mapping are given in Fig. 3. In most cases, the derived parameters for both the unperturbed normal and intruder configurations show gradual variation as functions of N . Rather significant changes in the parameters χ_ν and χ_π from $N = 58 - 62$ reflect the transition from the prolate to γ -soft shapes, as suggested at the SCMF level. A particularly large mixing strength ω for ^{114}Te reflects the pronounced γ softness in the PES. A negative Δ value for ^{114}Te is also of interest. The reason for this is that the normal oblate configuration gains large deformation energies due to the strong quadrupole-quadrupole interaction [see (8)], and that the prolate local minimum is very close in energy to the oblate global minimum (Fig. 1).

B. Low-energy spectra

Figure 4 depicts systematic of the excitation energies of low-lying states for $^{108-126}\text{Te}$. The experimental 2_1^+ energy level, shown in Fig. 4(a), exhibits gradual evolution with N and becomes lowest at $N = 68$. The observed 4_1^+ and 6_1^+ energy levels exhibit slightly different

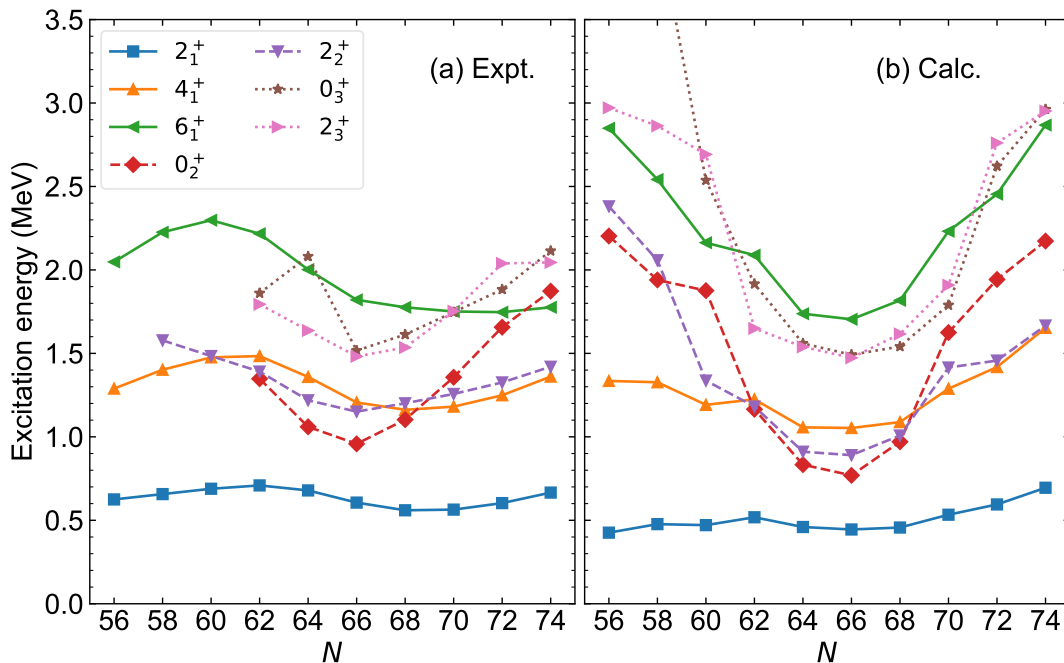


FIG. 4. (a) Experimental [20, 21, 71, 72] and (b) calculated excitation energies of low-lying states for the even-even $^{108-126}\text{Te}$ isotopes. The calculations are based on the IBM2-CM for $^{114-122}\text{Te}$, and on the IBM-2 with a single configuration for other nuclei.

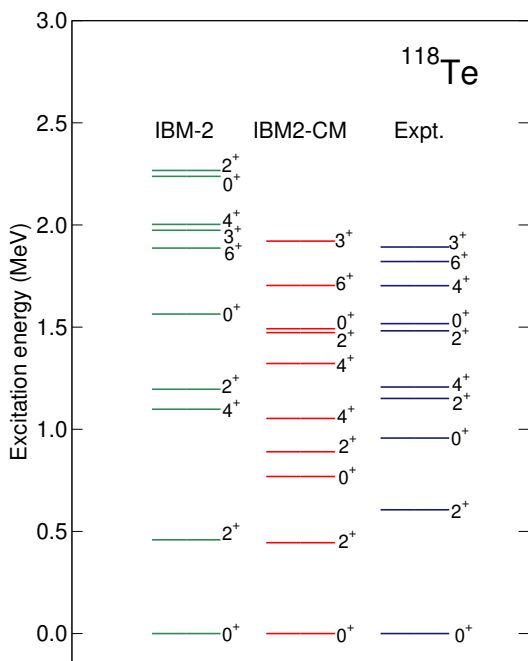


FIG. 5. Predicted low-energy spectra for ^{118}Te from the IBM-2 and IBM2-CM, and the experimental data [21].

patterns from that of the 2_1^+ level, that is, the 4_1^+ energy level exhibits a weak parabolic dependence on N ,

and the 6_1^+ level stays rather constant from $N = 68 - 74$. Experimentally, the 2_1^+ , 4_1^+ , and 6_1^+ levels exhibit inverse parabolas with maximal values at $N = 62$ (for the 2_1^+ and 4_1^+ states) and $N = 60$ (for the 6_1^+ state). The observed levels for the nonyrast states $0_{2,3}^+$ and $2_{2,3}^+$ exhibit a parabolic behavior, and become lowest in energy at the neutron midshell $N = 66$. The 0_2^+ and 2_3^+ energy levels are experimentally suggested to vary especially sharply.

Figure 4(b) shows the predicted excitations energies, obtained from the IBM2-CM for $^{114-122}\text{Te}$ and from the IBM-2 with a single configuration for the other Te nuclei. The IBM2-CM results for all spectroscopic properties discussed in the following are those obtained using the Δ values of (8). The overall systematic of the calculated 2_1^+ levels is rather consistent with the pattern observed experimentally. The calculated 4_1^+ energy levels exhibit a weak parabolic dependence on N . The calculated ratios $R_{4/2} = E(4_1^+)/E(2_1^+)$ of the 4_1^+ to 2_1^+ excitation energies take almost constant values $R_{4/2} \approx 2.3 - 2.4$ for $^{114-126}\text{Te}$, which are slightly larger than the experimental values $R_{4/2} \approx 2.0$. For the $^{108,110}\text{Te}$ nuclei, the IBM-2 calculation with a single (prolate) configuration yields a more rotational-like spectrum with the $R_{4/2}$ ratios, 3.13 and 2.78, respectively, which are higher than the experimental values $R_{4/2} = 2.06$ and 2.13. The differences are due to the fact that the RHB-SCMF PES exhibits a very sharp potential valley, and to reproduce this feature both the χ_ν and χ_π parameters have to be large in magnitude, being close to the SU(3) limit, $-\sqrt{7}/2$ [73], and

the resultant IBM-2 Hamiltonian produces a rotational-like spectrum. Furthermore, the IBM-2 space for a single configuration for these nuclei may be too restricted to describe reasonably the energy levels with spin $I \geq 6$. On the neutron-rich side with $N \geq 70$, the observed 4_1^+ systematic is more or less reproduced in the present calculation.

The 6_1^+ energy levels predicted in the IBM2-CM exhibit a stronger parabolic dependence on N than the 4_1^+ ones, but experimentally the 4_1^+ and 6_1^+ energy levels are quite similar in systematic. The quantitative differences between the 4_1^+ and 6_1^+ energy levels within the theory could be attributed to the facts that, as mentioned above, the boson model space becomes more restricted when approaching the neutron major shells $N = 50$ and 82 , pushing up higher-spin states with $I \geq 6$, and that the mixing in these low-lying states is so strong that significant degrees of level repulsion occur. The particularly low-lying experimental 6_1^+ energy level with respect to the 4_1^+ one on the neutron-rich side does not look like a typical collective band structure. To account for this energy-level pattern, some additional correlations, e.g., couplings to noncollective degrees of freedom, may need to be taken into account in the IBM framework.

The predicted nonyrast levels display a parabolic pattern and become particularly low in energy in the isotopes $^{114-120}\text{Te}$, with minimal energies at $N = 66$. This systematic resembles that of the experimental data and is considered to be a signature of the prolate-oblate shape coexistence.

Concerning the nuclei $^{114-122}\text{Te}$, the IBM-2 calculations using only a single oblate configuration produce the excitation energies for the yrast states that essentially do not differ from those within the IBM2-CM. Notable differences between the IBM2-CM and IBM-2 are found in that the IBM-2 generally produces the nonyrast levels that are much higher than those from the IBM2-CM. As an illustrative example, Fig. 5 shows low-energy spectra for ^{118}Te computed by the IBM2-CM and IBM-2. The IBM2-CM predicts low-lying 0_2^+ and 0_3^+ energy levels that are more consistent with experiment than the IBM-2. An improvement over the IBM-2 is that not only the excited 0^+ energy levels, but also the order of levels, except for the 4_2^+ level, appears to be reproduced better in the IBM2-CM.

Note also that the present IBM2-CM and IBM-2 results for the low-energy levels are qualitatively similar to those from the RHB+QCH calculations in Ref. [34], particularly the one that employed the default value of the pairing strengths constant for all isotopes. Some quantitative differences from the present results are that the QCH predicted the 2_1^+ , 4_1^+ , and 0_2^+ energy levels to be lowest at ^{116}Te , and produced a local inverse parabolic pattern of the 2_1^+ and 4_1^+ levels with maximal energies at $N = 58$ or 60 .

To see the importance of the configuration mixing, Table I gives overlap probabilities (in percent) of the basis states corresponding to the intruder boson space of

TABLE I. Contributions (in percent) of the intruder configurations in the IBM2-CM wave functions for low-spin states of $^{114-122}\text{Te}$.

	^{114}Te	^{116}Te	^{118}Te	^{120}Te	^{122}Te
0_1^+	40	21	9	15	3
0_2^+	63	81	91	86	96
0_3^+	46	11	6	11	3
2_1^+	48	30	12	18	3
2_2^+	56	64	82	70	14
2_3^+	55	34	22	36	87
4_1^+	57	54	33	31	4
6_1^+	69	78	79	62	7

$N_\pi = 3$ and the eigenfunctions of the IBM2-CM for low-spin states. From the table one can see that, in most of the states, significant degrees of intruder prolate contributions are present even in the yrast states. Particularly strong mixing is suggested for the low-lying states in ^{114}Te and ^{116}Te . For all those nuclei shown in the table, the 0_2^+ state mainly comes from the prolate intruder configuration. For ^{122}Te , the mixing is minor, and the intruder configuration does not seem to play an important role, except for the 0_2^+ and 2_3^+ wave functions.

C. Electromagnetic properties

Using the wave functions resulting from the mapped IBM2-CM Hamiltonian, transition properties for given states are computed. In the IBM2-CM, the $E2$ operator is given as

$$\hat{T}^{(E2)} = \sum_{i=1,3} \hat{P}_i (e_{\nu,i} \hat{Q}_{\nu,i} + e_{\pi,i} \hat{Q}_{\pi,i}) \hat{P}_i, \quad (9)$$

where $e_{\rho,i}$ and $\hat{Q}_{\rho,i}$ are neutron or proton effective charges and quadrupole operators (3) for the normal ($i = 1$) and intruder ($i = 3$) configurations, respectively. The effective charges, $e_{\nu,1} = e_{\pi,1} = 0.085$ eb and $e_{\nu,3} = e_{\pi,3} = 0.110$ eb, which are similar to those used for Cd isotopes [49], are adopted in the IBM2-CM. For the IBM-2, the boson charges $e_\nu = e_\pi = 0.095$ eb are employed so as to reproduce the overall systematic with N of the experimental $B(E2; 2_1^+ \rightarrow 0_1^+)$, $B(E2; 4_1^+ \rightarrow 2_1^+)$, and $B(E2; 6_1^+ \rightarrow 4_1^+)$ values. The $M1$ operator in the IBM2-CM reads

$$\hat{T}^{(M1)} = \sqrt{\frac{3}{4\pi}} \sum_{i=1,3} \hat{P}_i (g_{\nu,i} \hat{L}_\nu + g_{\pi,i} \hat{L}_\pi) \hat{P}_i, \quad (10)$$

where $\hat{L}_\rho = \sqrt{10} [d_\rho^\dagger \times \tilde{d}_\rho]^{(1)}$ is the boson angular-momentum operator. For the effective g factors $g_{\rho,i}$, the empirical values obtained in Ref. [19] are adopted: $g_{\nu,1} = g_{\nu,3} = 0.24 \mu_N$ (nuclear magneton) and $g_{\pi,1} = g_{\pi,3} = 0.5 \mu_N$.

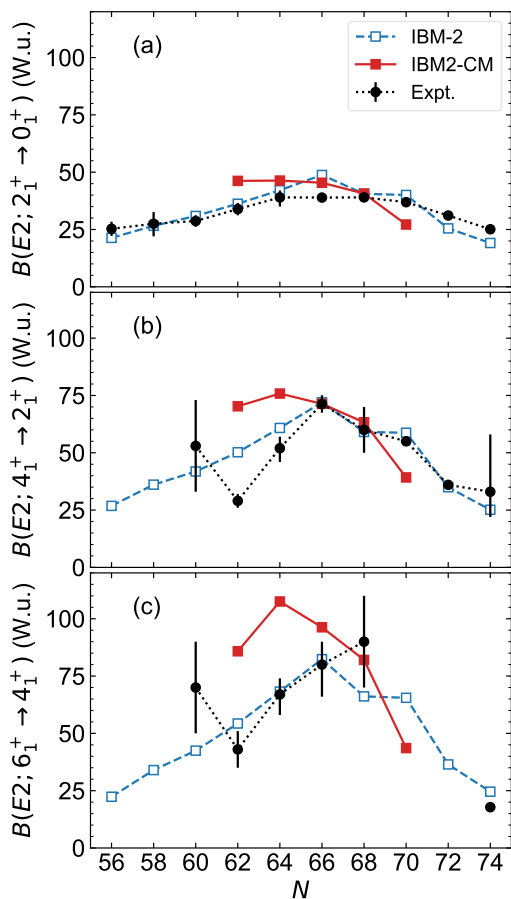


FIG. 6. (a) $B(E2; 2_1^+ \rightarrow 0_1^+)$, (b) $B(E2; 4_1^+ \rightarrow 2_1^+)$, and (c) $B(E2; 6_1^+ \rightarrow 4_1^+)$ values in Weisskopf units (W.u.) for Te isotopes calculated with the IBM2-CM and IBM-2. Experimental data are adopted from Refs. [21, 22, 24, 71, 72, 74–76]. See the main text for details.

Figure 6 exhibits calculated $B(E2; 2_1^+ \rightarrow 0_1^+)$, $B(E2; 4_1^+ \rightarrow 2_1^+)$, and $B(E2; 6_1^+ \rightarrow 4_1^+)$ values in Weisskopf units (W.u.) for the Te isotopes in the IBM2-CM and IBM-2. The $B(E2; 2_1^+ \rightarrow 0_1^+)$ data are adopted from Ref. [74] for ^{110}Te , Ref. [24] for ^{116}Te , Ref. [22] for ^{118}Te , and Ref. [76] for all the other Te isotopes. The data for the $B(E2; 4_1^+ \rightarrow 2_1^+)$ and $B(E2; 6_1^+ \rightarrow 4_1^+)$ values are taken from Ref. [72] for $^{112,114,120,122,124}\text{Te}$, Ref. [24] for ^{116}Te , and Ref. [71] for ^{126}Te . The experimental $B(E2; 4_1^+ \rightarrow 2_1^+)$ and $B(E2; 6_1^+ \rightarrow 4_1^+)$ values for ^{118}Te are adopted from Ref. [22] and Ref. [21], respectively.

From Fig. 6(a) one can observe gradual evolution of the experimental $B(E2; 2_1^+ \rightarrow 0_1^+)$ values. The IBM-2 reproduces this trend and gives the maximal $B(E2; 2_1^+ \rightarrow 0_1^+)$ value at the middle of the shell $N = 66$. In the IBM2-CM, the maximal $B(E2; 2_1^+ \rightarrow 0_1^+)$ value, 46.3 W.u., is obtained rather at $N = 64$, which is slightly larger than the recent experimental value 39_{-3}^{+4} W.u. [24] The IBM2-CM provides a particularly large $B(E2; 2_1^+ \rightarrow 0_1^+)$ value, 46.2 W.u., for ^{114}Te , which overestimates the experimen-

tal value [71]. The $4_1^+ \rightarrow 2_1^+$ transition rates are experimentally suggested to be maximal at the midshell $N = 66$. This behavior is reasonably reproduced by the IBM-2. The IBM2-CM provides for ^{118}Te and ^{120}Te the $B(E2; 4_1^+ \rightarrow 2_1^+)$ values that are consistent with the corresponding experimental values, 71.3 ± 9.8 W.u. [22] and 60 ± 10 W.u. [75], respectively.

What is worth noticing is a reduction of the observed $B(E2; 4_1^+ \rightarrow 2_1^+)$ value at ^{114}Te , being of the same order of magnitude as the $B(E2; 2_1^+ \rightarrow 0_1^+)$ value. This local pattern is not reproduced either by the IBM2-CM or IBM-2. Earlier IBM2-CM [19] and large-scale shell model (LSSM) [26] calculations also overestimated the $B(E2; 4_1^+ \rightarrow 2_1^+)$ value for ^{114}Te . The observed ratio $B_{4/2} = B(E2; 4_1^+ \rightarrow 2_1^+)/B(E2; 2_1^+ \rightarrow 0_1^+) < 1$ in ^{114}Te indicates a deviation from the interpretation in the collective model, in which $B_{4/2} > 1$ is expected. This feature resembles that found in heavier nuclei, e.g., ^{168}Os [79], which is often referred to as the $B(E2)$ anomaly. The anomalous reduction of $B(E2; 4_1^+ \rightarrow 2_1^+)$ at ^{114}Te has been reported in Refs. [80, 81], in which IBM calculations were performed assuming the pure vibrational $U(5)$ limit of the Hamiltonian. These IBM calculations reproduced energy spectra, but were unable to explain the $B(E2)$ systematic in question. The $B(E2)$ anomaly has been studied more recently with the IBM [82–84] that considered higher-order boson terms in the Hamiltonian. From symmetry-based analyses these studies indicated the importance of triaxiality for accounting for the anomalous $B(E2)$ systematic. The RHB-SCMF PES calculated in the present study for ^{114}Te suggests a pronounced γ softness (in Fig. 1). It is an interesting open question to study the influence of the γ softness on the $B(E2)$ values obtained from the IBM2-CM mapping that includes some additional interaction terms in the Hamiltonian, as has been made in the aforementioned calculations [82–84].

From Fig. 6(c) one can see that experimentally the behavior of the $B(E2; 6_1^+ \rightarrow 4_1^+)$ values is basically similar to that of the $B(E2; 4_1^+ \rightarrow 2_1^+)$, in particular, the local pattern at ^{114}Te . The present IBM-2 generally reproduces the experimental $B(E2; 6_1^+ \rightarrow 4_1^+)$ values for $^{114,116,118}\text{Te}$. One notices that in some cases the IBM-2 seem to give a better description of the $B(E2; 4_1^+ \rightarrow 2_1^+)$ and $B(E2; 6_1^+ \rightarrow 4_1^+)$ values than the IBM2-CM. These results may indicate that in the IBM mapping, at least in its current implementation, the inclusion of the configuration mixing does not necessarily lead to a complete description of the transition properties. For instance, the overestimates of the $B(E2; 4_1^+ \rightarrow 2_1^+)$ and $B(E2; 6_1^+ \rightarrow 4_1^+)$ values for ^{114}Te and ^{116}Te could be attributed to the fact that the considerable amounts of the deformed intruder configurations are included in both the 6_1^+ and 4_1^+ states (see Table I) and give rise to unexpectedly strong quadrupole collectivity.

Figure 7 shows the reduced $E2$ transition strengths for nonyrast states, $B(E2; 0_2^+ \rightarrow 2_1^+)$, $B(E2; 2_2^+ \rightarrow 2_1^+)$, $B(E2; 2_2^+ \rightarrow 0_2^+)$, and $B(E2; 2_3^+ \rightarrow 0_2^+)$. The calculated $B(E2; 0_2^+ \rightarrow 2_1^+)$ values in the IBM2-CM for ^{114}Te and

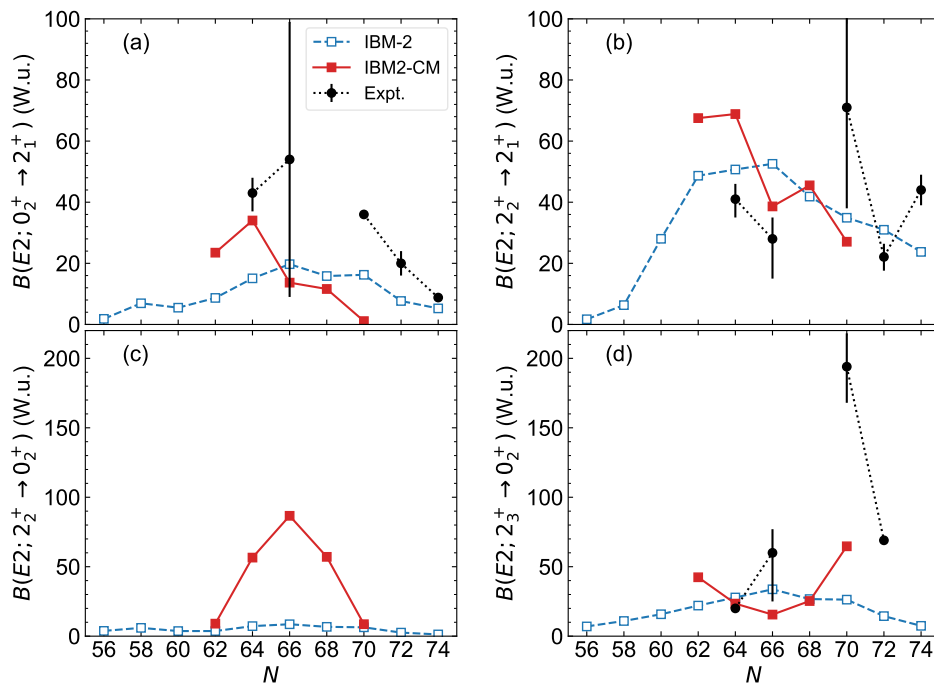


FIG. 7. Same as the caption to Fig. 6, but for the (a) $B(E2; 0_2^+ \rightarrow 2_1^+)$, (b) $B(E2; 2_2^+ \rightarrow 2_1^+)$, (c) $B(E2; 2_2^+ \rightarrow 0_2^+)$, and (d) $B(E2; 2_3^+ \rightarrow 0_2^+)$ values. Experimental data are taken from Refs. [20, 21, 77, 78]. The experimental $B(E2; 2_3^+ \rightarrow 0_2^+)$ value for ^{116}Te is a lower limit, > 20 W.u. [20]. Also the experimental $B(E2; 0_2^+ \rightarrow 2_1^+)$ value for ^{122}Te [77], and $B(E2; 2_2^+ \rightarrow 2_1^+)$ and $B(E2; 2_3^+ \rightarrow 0_2^+)$ values for ^{124}Te [78] are upper limits.

^{116}Te are rather large, reflecting the strong mixing of the oblate and prolate shapes. For ^{116}Te , in particular, the IBM2-CM value of $B(E2; 0_2^+ \rightarrow 2_1^+)$ is of the same order of magnitude as the experimental value 43_{-5}^{+6} W.u. While the $0_2^+ \rightarrow 2_1^+$ transition is expected to be large for the midshell nuclei in which configuration mixing is supposed to play a relevant role, in both the IBM2-CM and IBM-2 this transition is suggested to be rather weak for $^{118,120,122}\text{Te}$. For the IBM-2, this is probably related to the fact that the 0_2^+ energy levels are predicted to be systematically much higher than the experimental ones (see Fig. 5 in the case of ^{118}Te). In the IBM2-CM, the underestimates of $B(E2; 0_2^+ \rightarrow 2_1^+)$ for $^{118,120,122}\text{Te}$ can be explained in terms of the difference in structure of the wave functions for the 0_2^+ and 2_1^+ states: the intruder configuration dominates nearly 90% of the 0_2^+ wave function, but makes a less significant, $< 20\%$, contribution to the 2_1^+ wave function (see Table 1). One should also notice that the experimental $B(E2; 0_2^+ \rightarrow 2_1^+)$ value obtained for ^{118}Te in Ref. [21] has a large error bar, and that only the upper limit is known experimentally for ^{122}Te [77].

In Fig. 7(b), the IBM-2 appears to give a reasonable description of the $B(E2; 2_2^+ \rightarrow 2_1^+)$ values. The corresponding IBM2-CM values for ^{114}Te and ^{116}Te are considerably larger than those of the IBM-2, reflecting enhanced configuration mixing effects for these states.

In Fig. 7(c), the IBM2-CM predicts enhanced E2 transitions $2_2^+ \rightarrow 0_2^+$ for the nuclei $^{116,118,120}\text{Te}$, while the

IBM-2 gives only vanishing $B(E2; 2_2^+ \rightarrow 0_2^+)$ values for all the Te nuclei. In the IBM2-CM, the level structure shown in Fig. 4(b) and the strong $2_2^+ \rightarrow 0_2^+$ transitions imply that the 0_2^+ state is the bandhead of the excited 0^+ band and that the 2_2^+ state is a member of that band.

One observes in Fig. 7(d) that the IBM2-CM gives strong E2 transitions $2_3^+ \rightarrow 0_2^+$ for ^{114}Te and ^{122}Te . From this and the energy-level structure shown in Fig. 4(b), the IBM2-CM suggests for these nuclei a possible 0^+ excited band with the bandhead 0_2^+ and with the 2_3^+ state being a member of the band. Experimentally, the 1482-keV level in ^{118}Te was assigned to be the 2_3^+ state, and $B(E2; 2_3^+ \rightarrow 0_2^+) = 60_{-17}^{+30}$ W.u. was extracted. The measured $B(E2; 2_3^+ \rightarrow 0_2^+)$ value for ^{122}Te [77], 194_{-24}^{+26} W.u., is quite large. The IBM-2 typically gives $B(E2; 2_3^+ \rightarrow 0_2^+) \approx 5 \sim 25$ W.u. For the midshell nucleus ^{118}Te , the IBM-2 value of $B(E2; 2_3^+ \rightarrow 0_2^+)$ is larger than that of the IBM2-CM and is within the error bar of the experimental data [21].

In the RHB+QCH calculation of Ref. [34], the $B(E2; 2_1^+ \rightarrow 0_1^+)$ values were of the same order of magnitude as those from the present IBM2-CM and IBM-2, but the QCH values of $B(E2; 4_1^+ \rightarrow 2_1^+)$ were systematically larger than the present results nearly by a factor of 2. Both the $B(E2; 2_1^+ \rightarrow 0_1^+)$ and $B(E2; 4_1^+ \rightarrow 2_1^+)$ values in the QCH exhibited increasing patterns toward ^{116}Te , at which nucleus maximal values were ob-

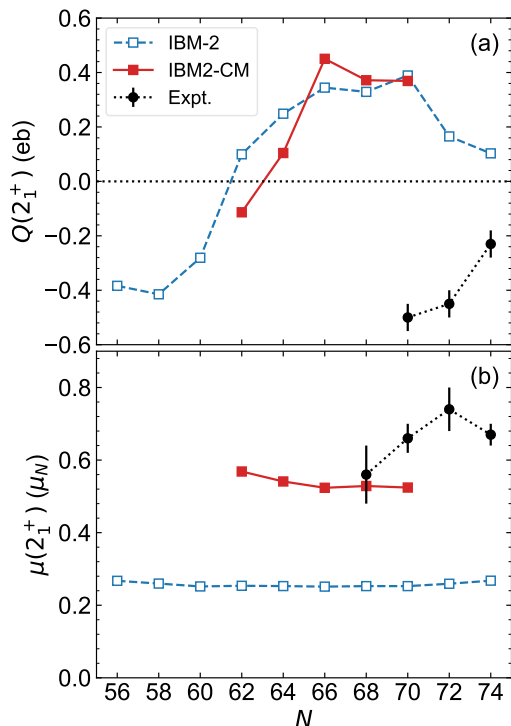


FIG. 8. (a) Spectroscopic electric quadrupole moments and (b) magnetic dipole moments for the 2_1^+ state for the Te isotopes. The calculated results from the IBM-2 and IBM2-CM are shown. Experimental data are taken from ENSDF database [71].

tained. The RHB+QCH suggested considerably larger $B(E2; 0_2^+ \rightarrow 2_1^+)$ than the present IBM2-CM and IBM-2 calculations for all the Te isotopes considered here, with a maximal value, $B(E2; 0_2^+ \rightarrow 2_1^+) > 100$ W.u., being reached at ^{116}Te .

Figure 8 shows calculated spectroscopic quadrupole moment $Q(2_1^+)$ (in eb) and magnetic dipole moment $\mu(2_1^+)$ for the 2_1^+ states. The IBM2-CM and IBM-2 both show a change in sign of the $Q(2_1^+)$ values from $N = 60$ to 62 and $N = 62$ to 64, reflecting the transition from the prolate to oblate shapes. For $^{122-126}\text{Te}$, the calculated $Q(2_1^+)$ values are opposite in sign to the experimental values [71]. Earlier IBM2-CM calculations provided negative $Q(2_1^+)$ values for most of the Te nuclei with mass $A \geq 112$. The previous RHB+QCH model also predicted $Q(2_1^+) < 0$ for ^{116}Te and ^{118}Te [34]. The discrepancy shown in Fig. 8(a) appears to arise from the fact that the RHB-SCMF PES exhibit an oblate minimum, since in the IBM-2 mapping framework, the sign of the $Q(2_1^+)$ moment depends on whether the SCMF energy minimum is on the oblate or prolate side. For the oblate deformation, the χ_ν and χ_π parameters in the quadrupole operator are chosen to satisfy the sum $\chi_\nu + \chi_\pi > 0$, hence the positive $Q(2_1^+)$ values are obtained. If one employs other relativistic EDFs, e.g., density-dependent meson-

exchange (DD-ME2) EDF [85], the corresponding PESs for most of the Te isotopes exhibit an oblate global minimum [28, 34] as in the case of the DD-PC1 functional, which is used here. The Hartree-Fock-Bogoliubov calculations [32] with the Gogny-D1S EDF [86], predicted a prolate global minimum from ^{108}Te up to ^{120}Te , but an essentially nearly spherical shape for $^{122-126}\text{Te}$. The IBM2-CM values for the $\mu(2_1^+)$ moments for the mid-shell nuclei $^{114-122}\text{Te}$ are substantially larger than those from the IBM-2. The larger $\mu(2_1^+)$ values in the IBM2-CM than those in the IBM-2 may be considered to be a characteristic effect of the mixing. However, given that the 2_1^+ states in heavier Te nuclei with $N = 70$ to 74 are predicted to be oblate in nature in both the IBM-2 and IBM2-CM, as opposed to the experimental data [see Fig. 8(a)], the structure of the 2_1^+ states may not be properly described in the present IBM mapping calculations, whether the configuration mixing is considered or not. The predicted magnetic moments $\mu(2_1^+)$ in Fig. 8(b) are thus approximate.

The IBM2-CM produces a number of lower-spin nonyrast states at low energy. The electromagnetic transition properties of these states are expected to help distinguishing intruder states from vibrational states in nuclei in this mass region. In recent years, extensive experimental work has been made on possible shape coexistence effects on low-lying states in the neighboring midshell Sn isotopes: $^{112,114}\text{Sn}$ [16], ^{116}Sn [17], and ^{118}Sn [18]. In these studies, the IBM2-CM calculations were performed with parameters being fitted to data. Comparisons of the IBM2-CM results of the $B(E2)$ values for nonyrast states revealed that the data followed to a good extent the $E2$ selection rules required by dynamical symmetries of the IBM, but this was not the case for some states with specific spin, e.g., 3_1^+ and $4_{3,4,5}^+$ states in ^{116}Sn [17]. The authors of the above studies attributed these discrepancies to some missing elements in the IBM-2 wave functions, indicating some deficiency of the IBM2-CM framework in reproducing the detailed $B(E2)$ systematic.

As shown in Figs. 6 and 7, difficulties in reproducing the $B(E2)$ values with the mapped IBM2-CM appear even for low-lying states. This is, however, not surprising since the IBM2-CM parameters are here obtained from the SCMF mapping procedure rather than directly fitting to the experimental data, and since the derived parameters as well as the form of the Hamiltonian are considerably different from those that furnish certain (dynamical) symmetries leading to the expected $E2$ selection rules. In addition, significant degree of configuration mixing is present in the relevant wave functions for low-lying states, which makes it highly nontrivial to firmly conclude whether the states are oblate or prolate in nature. It seems to be, therefore, beyond the scope of the present work to reproduce all details of the $B(E2)$ systematic and selections rules accurately.

Electric monopole ($E0$) transitions between 0^+ states are another signature for the configuration mixing in the studied mass region. In the neighboring Sn isotopes,

for example, a recent measurement [87] reported a large $\rho^2(E0; 0_3^+ \rightarrow 0_2^+)$ value for ^{120}Sn , indicating strong mixing between the 0_2^+ and 0_3^+ states. Within the IBM2-CM, the $E0$ operator is given as

$$\hat{T}^{(E0)} = \sum_{i=1,3} \hat{P}_i (a_{\nu,i} \hat{n}_{d\nu} + a_{\pi,i} \hat{n}_{d\pi}) \hat{P}_i, \quad (11)$$

where $\hat{n}_{d\rho}$ represents the neutron or proton d -boson number operator (3), and $a_{\rho,i}$ are corresponding parameters. The formula (11) should, in principle, contain additional terms that depend only on the neutron and proton boson numbers fixed for a given nucleus for both configurations. These additional terms are relevant to study intrinsic quantities like charge radii, but do not contribute to excited states, hence omitted in the following discussion, which is rather focused on the $E0$ transitions.

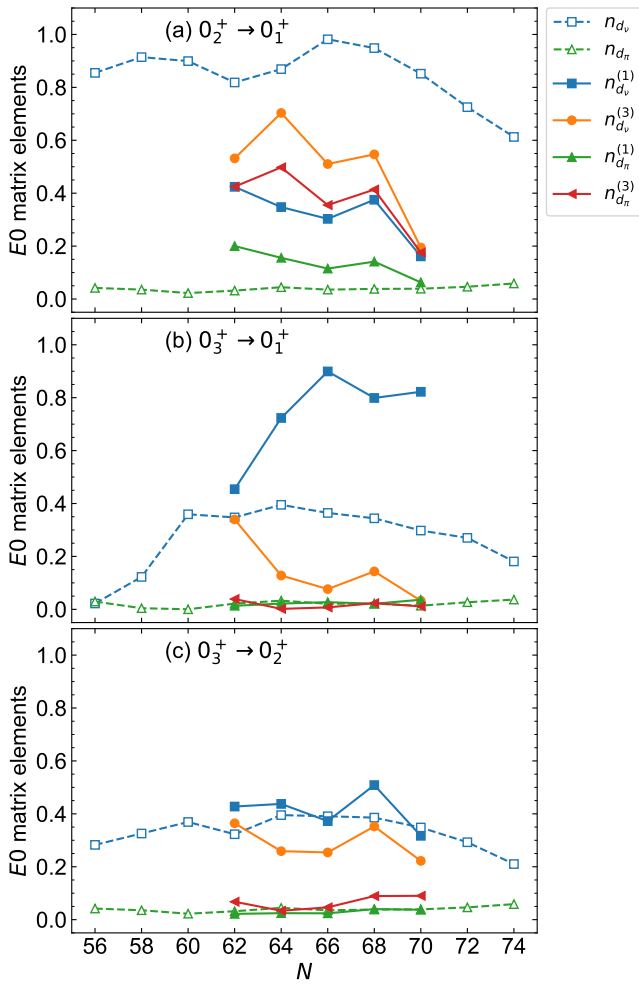


FIG. 9. Matrix elements of terms in the $E0$ operator for the IBM2-CM and those for the IBM-2 for the $0_2^+ \rightarrow 0_1^+$, $0_3^+ \rightarrow 0_1^+$, and $0_3^+ \rightarrow 0_2^+$ transitions in Te isotopes. See the main text for details.

Figure 9 depicts absolute values of matrix elements of four terms in the $E0$ operator (11) denoted $n_{d\rho}^{(i)}(0_k^+ \rightarrow$

$0_l^+) \equiv |\langle 0_l^+ | \hat{P}_i \hat{n}_{d\rho} \hat{P}_i | 0_k^+ \rangle|$, which are calculated for the $0_2^+ \rightarrow 0_1^+$, $0_3^+ \rightarrow 0_1^+$, and $0_3^+ \rightarrow 0_2^+$ transitions in the IBM2-CM. These values are also compared with the equivalent matrix elements in the IBM-2, defined as $n_{d\rho}(0_k^+ \rightarrow 0_l^+) \equiv |\langle 0_l^+ | \hat{n}_{d\rho} | 0_k^+ \rangle|$. It is seen from Fig. 9 that in the IBM-2 there is essentially no proton contribution to all three $E0$ transitions, and that the neutron component $n_{d\nu}(0_2^+ \rightarrow 0_1^+)$ is larger than $n_{d\nu}(0_3^+ \rightarrow 0_1^+)$ and $n_{d\nu}(0_3^+ \rightarrow 0_2^+)$ values by a factor of 2-3. In the IBM2-CM, contributions from protons for the normal and intruder configurations, $n_{d\pi}^{(1,3)}(0_3^+ \rightarrow 0_1^+)$ and $n_{d\pi}^{(1,3)}(0_3^+ \rightarrow 0_2^+)$, are basically negligible for the $^{114-122}\text{Te}$ nuclei. The four components $n_{d\rho}^{(1,3)}$ appear to make sizable amounts of contributions to the $0_2^+ \rightarrow 0_1^+$ transition in the IBM2-CM. It is of interest that the neutron and proton terms for the intruder configurations, $n_{d\rho}^{(3)}(0_2^+ \rightarrow 0_1^+)$, make larger contributions to the $0_2^+ \rightarrow 0_1^+$ transition than those for the normal configuration, $n_{d\rho}^{(1)}(0_2^+ \rightarrow 0_1^+)$, and this finding implies that configuration mixing plays an important role in the $0_2^+ \rightarrow 0_1^+$ transition. The $0_3^+ \rightarrow 0_1^+$ transition is, however, shown to be dominated by the contribution from neutrons in the normal configuration, except for ^{114}Te . For the ^{114}Te nucleus, the neutron d -boson terms in the intruder configuration also makes a larger contribution to the $0_3^+ \rightarrow 0_1^+$ transition, illustrating the strong configuration mixing in this nucleus in the present calculation (see also Table I). From Fig. 9(b) it is seen that the $0_3^+ \rightarrow 0_2^+$ decay is accounted for mainly by the matrix elements $n_{d\nu}^{(1)}(0_3^+ \rightarrow 0_2^+)$ and $n_{d\nu}^{(3)}(0_3^+ \rightarrow 0_2^+)$. The fact that the latter is of the same order of magnitude as the former again indicates importance of configuration mixing in the $0_3^+ \rightarrow 0_2^+$ transition.

To compare with observable $E0$ properties, e.g., $\rho^2(E0)$ values, four parameters $a_{\nu,1}$, $a_{\nu,3}$, $a_{\pi,1}$, and $a_{\pi,3}$ in the $E0$ parameters need to be determined. It is, however, not obvious to find optimal and fixed values of these parameters that can be used for all the considered Te isotopes. This is partly because the experimental information of the $E0$ transition properties, which can provide constraints for the $E0$ parameters, is not as abundant as in the case of the neighboring Sn and Cd nuclei. As compared with the $E2$ and $M1$ transition properties, the $E0$ transitions have not been extensively studied in the IBM, and the parameters for the IBM $E0$ operator appropriate to reproduce the observed $E0$ properties have not been very well known. In addition, as shown in Fig. 9 the calculated matrix elements of the terms in the $E0$ operator are rather sensitive to the structure of the wave functions of the initial and final 0^+ states. The ambiguity of the $E0$ parameters was indeed pointed out in the empirical IBM2-CM calculation in Ref. [19], in which the $E0$ parameters fitted to reproduce the measured $\rho^2(E0)$ values for ^{122}Te and ^{124}Te differ significantly.

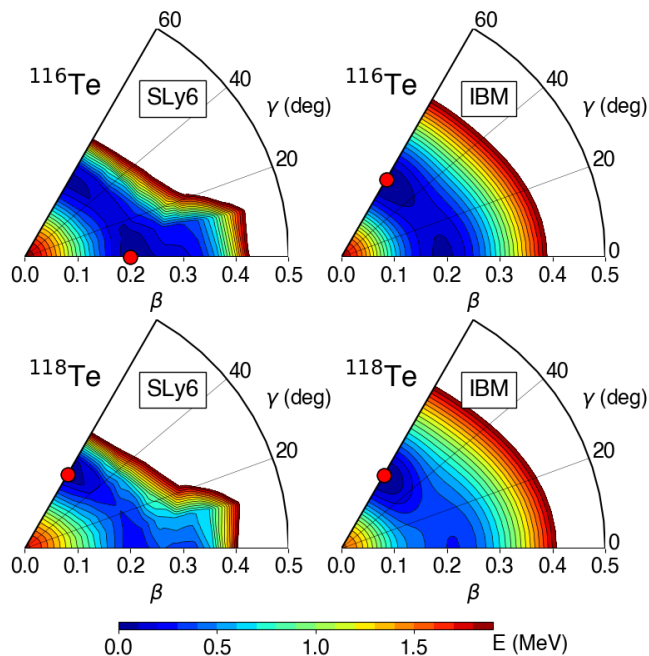


FIG. 10. SCMF PESs for ^{116}Te and ^{118}Te computed by the constrained HF+BCS method using the Skyrme SLy6 EDF, and the corresponding IBM2-CM PESs.

D. Dependence on the EDF

As has been pointed out above, even though many of the SCMF calculations for the near midshell Te isotopes have indicated the appearance of prolate and oblate minima in the energy surface, the prolate-oblate energy balance and γ softness seem to be at variance with mean-field calculations using different functionals. Results of the present IBM2-CM calculations for low-energy properties should, therefore, depend on the choice of the EDF that underlies the mapping procedure.

As an illustrative example, Fig. 10 shows the energy surfaces for ^{116}Te and ^{118}Te obtained from the constrained Hartree-Fock plus BCS (HF+BCS) method [88, 89] using the Skyrme SLy6 EDF [90]. For the pairing channel, the density-dependent zero-range pairing force with the strength of 1000 MeV fm^3 truncated below and above the Fermi surface by 5 MeV for both protons and neutrons is adopted. For ^{116}Te , the global minimum is obtained on the prolate side, which, however, is only 14 keV in energy below the minimum on the oblate side. For ^{118}Te , the prolate minimum corresponds to the global minimum, while there are two prolate local minima. Similarly to the RHB results shown in Fig. 1, the HF+BCS calculations predict for both nuclei the coexistence of prolate and oblate minima in the PESs, but the Skyrme HF+BCS energy surfaces are much softer in the γ deformation than the RHB ones. The mapped IBM2-CM PES for ^{116}Te reproduces the original HF+BCS PES, but produces the global minimum on the oblate side. This

is a consequence of the configuration mixing of the PESs for the two unperturbed spaces (5), which could alter the energy of the prolate minimum to be slightly lower than that of the prolate global minimum, especially when the two minima are quite close in energy. As for ^{118}Te , the normal configuration is associated with the oblate global minimum, and the intruder configuration with the prolate minimum corresponding to the smaller $\beta \approx 0.2$ deformation. The third minimum at $\beta \approx 0.3$ could also have impacts on the final results, but is neglected here, since the present calculation is restricted to the mixing of two configurations and also for the sake of simplicity.

In Fig. 11, the low-energy spectra obtained from the IBM2-CM using the Skyrme-SLy6 EDF are compared with those employing the DD-PC1 EDF in the RHB calculations. With the SLy6 EDF as a microscopic input for the IBM2-CM, the resultant energy spectrum is rather compressed as compared with the one using the DD-PC1. The reason for this to occur is that the present HF+BCS calculation with the SLy6 EDF suggests a steeper potential valley along the β deformation in the PES, requiring a larger quadrupole-quadrupole strength, than the RHB with the DD-PC1 force. In addition, the 2_3^+ and 3_1^+ energy-levels in the Skyrme-SLy6 mapped IBM2-CM are particularly lower than the DD-PC1 counterparts. These states are supposed to be members of γ -vibrational bands in the present IBM2-CM calculations, and are rather low in energy when the Skyrme-SLy6 PESs are considered as inputs, which are γ softer than the DD-PC1 ones.

The degree of configuration mixing is also more significant in the Skyrme-SLy6 IBM2-CM than in the case of the DD-PC1 EDF. For instance, the intruder prolate configuration accounts for 48% (30%), 54% (71%), 50% (71%), 59% (42%), 61% (62%), 71% (63%) of the wave functions for the 0_1^+ , 0_2^+ , 0_3^+ , 2_1^+ , 2_2^+ , and 4_1^+ states for ^{116}Te (^{118}Te), respectively; these fractions are closer to 50% than for the DD-PC1 results (see Table I).

Tables II and III compare the $B(E2)$ and $B(M1)$ values, electric quadrupole and magnetic dipole moments resulting from the Skyrme-SLy6 mapped IBM2-CM with those from the DD-PC1 mapped IBM2-CM calculations. The boson effective charges for the $E2$ operator and effective g factors for the $M1$ operator in the case of the SLy6 input are chosen to be the same as those for the DD-PC1 case, but an overall factor is multiplied for the $E2$ operator so that the $B(E2; 2_1^+ \rightarrow 0_1^+)$ values should be equal to those from the DD-PC1 RHB calculations. The IBM2-CM with two different microscopic inputs overall give similar results. There are also several notable differences. For instance, the $B(E2; 0_3^+ \rightarrow 2_2^+)$ values relative to $B(E2; 0_3^+ \rightarrow 2_1^+)$ are larger with the SLy6 input than with the DD-PC1 input for both nuclei. Also, the sign $Q(2_1^+) < 0$ in the SLy6-mapped IBM2-CM for ^{116}Te , while it is positive in the DD-PC1 case. These differences between the IBM2-CM calculations with the different EDF inputs are attributed to the softness in the triaxial γ deformation of the SCMF PESs, since the γ softness influences the degree of the shape configuration

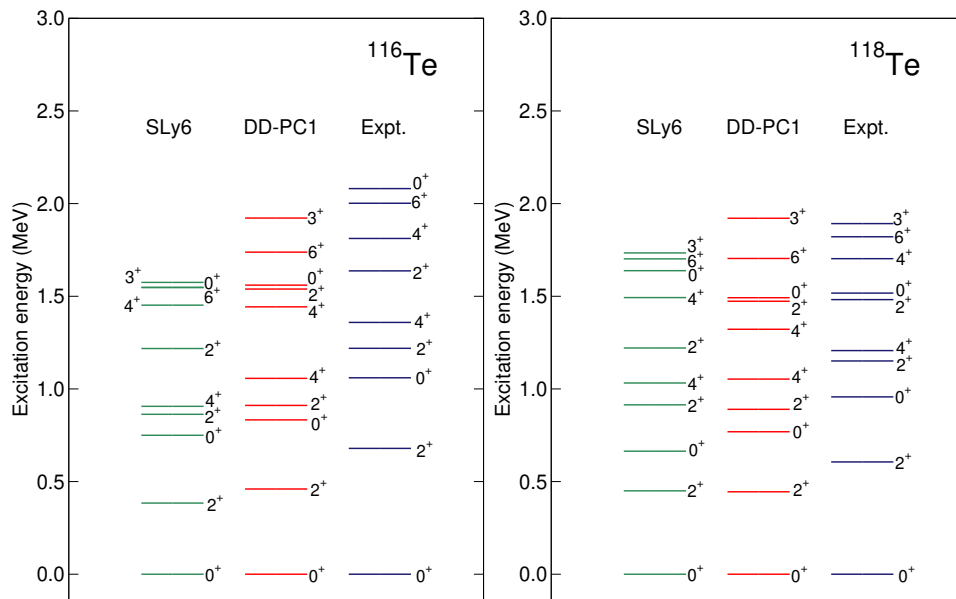


FIG. 11. Comparisons of low-energy spectra for ^{116}Te and ^{118}Te resulting from the IBM2-CM mapping with the Skyrme SLy6 force to those from the DD-PC1 force in the relativistic framework. Experimental data are adopted from Refs. [20, 71].

mixing.

IV. SUMMARY AND CONCLUSIONS

Evolution and coexistence of the intrinsic shapes and related low-energy spectroscopic properties in the even-even Te isotopes have been investigated. The IBM2-CM has been employed to distinguish possible intruder states from the low-lying states in midshell nuclei $^{114-122}\text{Te}$. The interaction strengths in the Hamiltonian of the IBM2-CM have been determined for each nucleus by mapping the RHB-SCMF PES with a given EDF and a pairing interaction onto the equivalent energy surface of the IBM2-CM. From the systematic of the calculated PESs the transition from the prolate to oblate shapes was suggested to occur at ^{114}Te , and a pronounced oblate-prolate shape coexistence was found in $^{116,118,120}\text{Te}$.

The calculated low-energy levels for the 0_2^+ , 2_2^+ , 0_3^+ , and 2_3^+ states exhibit parabolic behaviors with the lowest energies at the midneutron-shell nucleus ^{118}Te , which behaviors are characteristics of the emergent shape-coexistence structure observed in the neighboring Sn and Cd isotopic chains. To reproduce the observed systematic of the nonyrast energy levels, it appears to be reasonable to take into account the configuration mixing in the IBM framework. In many of the low-energy and low-spin states particularly in the $^{114-120}\text{Te}$ nuclei, the intruder configurations that are associated with the prolate shape having a large quadrupole deformation were shown to play an important role. Large predicted $B(E2)$ values such as $B(E2; 0_2^+ \rightarrow 2_1^+)$ and $B(E2; 2_2^+ \rightarrow 2_1^+)$, particularly at ^{114}Te and ^{116}Te , are also signatures of configu-

ration mixing. The predicted low-energy level structure and $E2$ transitions in the midshell region suggest a band built on the 0_2^+ state with a possible member being the 2_2^+ or 2_3^+ state. The 0_2^+ states in the present calculations were shown to be characterized by large amounts of the intruder configurations. Concerning the $E2$ transitions of the yrast states, however, in some cases the standard IBM-2 description with only a single configuration was shown to be adequate to reasonably reproduce the experimental data in comparison with the IBM2-CM. The inclusion of the configuration mixing, therefore, appears not to lead to complete descriptions of these transition properties, since the intruder configuration is to a great extent included in the corresponding wave functions and the admixture of the normal and intruder configurations makes it less obvious to properly account for the expected transition patterns in detail.

In particular, difficulties arose in reproducing the anomalous reduction of the $B(E2; 4_1^+ \rightarrow 2_1^+)$ and $B(E2; 6_1^+ \rightarrow 4_1^+)$ values at ^{114}Te , as observed experimentally. Neither of the present IBM2-CM and standard IBM-2, which are based on the microscopic EDF, and conventional IBM2-CM with parameters fitted to data, was not able to account for that phenomenon. The local systematic of these $E2$ transitions thus suggests that certain extensions of the IBM framework in general are in order for realistic nuclear structure studies. This will be a challenging, but interesting future study for a further development of the IBM2-CM that is based on the EDF. Furthermore, the calculated spectroscopic quadrupole moments suggested that the 2_1^+ states in heavier Te were oblate in nature, which is inconsistent with experiment. These results indicate that the struc-

TABLE II. Calculated $B(E2)$ and $B(M1)$ values (in W.u.), $Q(2_{1,2}^+)$ (in eb), and $\mu(2_1^+)$ (in μ_N) moments for ^{116}Te obtained from the IBM2-CM using the DD-PC1 and SLy6 EDFs as inputs. Experimental data are taken from Refs. [20, 24, 71].

	IBM2-CM		Experiment
	DD-PC1	SLy6	
$B(E2; 2_1^+ \rightarrow 0_1^+)$	46	46	39_{-3}^{+4}
$B(E2; 4_1^+ \rightarrow 2_1^+)$	76	71	52_{-5}^{+6}
$B(E2; 2_2^+ \rightarrow 0_1^+)$	0.6	0.09	
$B(E2; 2_2^+ \rightarrow 0_2^+)$	57	14	
$B(E2; 2_2^+ \rightarrow 2_1^+)$	69	65	41_{-5}^{+6}
$B(E2; 2_3^+ \rightarrow 0_1^+)$	0.09	0.7	
$B(E2; 2_3^+ \rightarrow 0_2^+)$	23	30	> 20
$B(E2; 2_3^+ \rightarrow 2_1^+)$	7	6	> 3
$B(E2; 2_3^+ \rightarrow 2_2^+)$	7	2	
$B(E2; 3_1^+ \rightarrow 2_2^+)$	28	45	
$B(E2; 4_2^+ \rightarrow 2_1^+)$	0.1	0.1	> 0.7
$B(E2; 4_2^+ \rightarrow 2_2^+)$	80	48	> 5
$B(E2; 4_2^+ \rightarrow 4_1^+)$	59	36	
$B(E2; 6_1^+ \rightarrow 4_1^+)$	108	88	67_{-9}^{+7}
$B(E2; 0_2^+ \rightarrow 2_1^+)$	34	27	43_{-5}^{+6}
$B(E2; 0_3^+ \rightarrow 2_1^+)$	14	3	
$B(E2; 0_3^+ \rightarrow 2_2^+)$	14	45	
$B(M1; 2_2^+ \rightarrow 2_1^+)$	3.60×10^{-4}	2.64×10^{-4}	$6_{-5}^{+6} \times 10^{-4}$
$B(M1; 2_3^+ \rightarrow 2_1^+)$	4.20×10^{-5}	3.88×10^{-4}	> 0.01
$B(M1; 2_3^+ \rightarrow 2_2^+)$	2.82×10^{-4}	2.00×10^{-6}	
$B(M1; 3_1^+ \rightarrow 2_1^+)$	1.20×10^{-5}	1.00×10^{-6}	
$B(M1; 3_1^+ \rightarrow 2_2^+)$	1.53×10^{-4}	3.60×10^{-5}	
$B(M1; 3_1^+ \rightarrow 4_1^+)$	1.27×10^{-4}	3.20×10^{-5}	
$B(M1; 4_2^+ \rightarrow 4_1^+)$	1.77×10^{-3}	1.03×10^{-3}	
$Q(2_1^+)$	0.14	-0.10	
$Q(2_2^+)$	-0.67	-0.14	
$\mu(2_1^+)$	0.54	0.56	

ture of the 2_1^+ states may not be correctly described. The spectroscopic results of the IBM2-CM are also influenced by a particular choice of the underlying EDF, since especially the prolate-oblate energy balance in the PES depends largely on the properties of the EDF. In some particular cases, the IBM2-CM combined with a given choice of the EDF may not be adequate to describe very accurately the observed spectroscopic properties. Certain improvements of the methodology are in order at the SCMF and/or IBM levels.

The results obtained from the present IBM2-CM calculations indicate the relevance of the intruder configurations and their couplings to the low-lying states in the mid-neutron-shell and neutron-deficient nuclei in the region with $Z > 50$. The present theoretical analysis can be extended to provide predictions on nuclear spectroscopy related to shape coexistence in other mass regions, which have been previously beyond reach of microscopic nuclear

structure models. This will be a step toward establishing a comprehensive picture of the shape coexistence in nuclei.

TABLE III. Same as the caption to Table II, but for ^{118}Te . Experimental data are taken from Refs. [21, 22, 71].

	IBM2-CM		Experiment
	DD-PC1	SLy6	
$B(E2; 2_1^+ \rightarrow 0_1^+)$	45	45	38.93 ± 0.98
$B(E2; 4_1^+ \rightarrow 2_1^+)$	71	74	71.3 ± 3.8
$B(E2; 2_2^+ \rightarrow 0_1^+)$	1.0	0.4	$1.8_{-0.4}^{+0.7}$
$B(E2; 2_2^+ \rightarrow 0_2^+)$	87	38	
$B(E2; 2_2^+ \rightarrow 2_1^+)$	39	51	28_{-7}^{+13a}
			264_{-57}^{+100b}
$B(E2; 2_3^+ \rightarrow 0_1^+)$	0.1	0.07	$0.20_{-0.05}^{+0.11}$
$B(E2; 2_3^+ \rightarrow 0_2^+)$	16	21	60_{-17}^{+35}
$B(E2; 2_3^+ \rightarrow 2_1^+)$	15	23	$3.4_{-0.9}^{+1.9c}$
			30_{-7}^{+16d}
$B(E2; 2_3^+ \rightarrow 2_2^+)$	3	0.9	$9.5_{-3.5}^{+8.5e}$
			166_{-61}^{+119f}
$B(E2; 3_1^+ \rightarrow 2_1^+)$	0.7	0.03	< 0.036
$B(E2; 3_1^+ \rightarrow 2_2^+)$	20	29	< 0.7
$B(E2; 3_1^+ \rightarrow 4_1^+)$	17	26	< 4.5
$B(E2; 4_2^+ \rightarrow 2_1^+)$	0.7	0.01	< 1.1
$B(E2; 4_2^+ \rightarrow 2_2^+)$	116	65	< 210
$B(E2; 4_2^+ \rightarrow 4_1^+)$	59	32	< 160
$B(E2; 6_1^+ \rightarrow 4_1^+)$	96	101	80_{-10}^{+14}
$B(E2; 0_2^+ \rightarrow 2_1^+)$	14	33	54 ± 45
$B(E2; 0_3^+ \rightarrow 2_1^+)$	22	10	1.3 ± 0.2
$B(E2; 0_3^+ \rightarrow 2_2^+)$	5	15	100
$B(M1; 2_2^+ \rightarrow 2_1^+)$	1.40×10^{-4}	3.68×10^{-4}	$9.5_{-2.1}^{+3.5} \times 10^{-2a}$
			$8.5_{-2.8}^{+3.5} \times 10^{-4b}$
$B(M1; 2_3^+ \rightarrow 2_1^+)$	2.00×10^{-6}	1.43×10^{-4}	$2.8_{-0.6}^{+1.4} \times 10^{-2c}$
			$1.3_{-0.5}^{+0.6} \times 10^{-4d}$
$B(M1; 2_3^+ \rightarrow 2_2^+)$	1.69×10^{-4}	2.10×10^{-5}	$2.4_{-0.9}^{+1.8} \times 10^{-2e}$
			$1.2_{-0.5}^{+0.9} \times 10^{-3f}$
$B(M1; 3_1^+ \rightarrow 2_1^+)$	3.00×10^{-6}	1.84×10^{-7}	$< 1.6 \times 10^{-3}$
$B(M1; 3_1^+ \rightarrow 2_2^+)$	1.26×10^{-4}	1.80×10^{-5}	$< 1.8 \times 10^{-2}$
$B(M1; 3_1^+ \rightarrow 4_1^+)$	6.50×10^{-5}	2.50×10^{-5}	$< 1 \times 10^{-2}$
$B(M1; 4_2^+ \rightarrow 4_1^+)$	1.20×10^{-3}	1.40×10^{-3}	< 0.018
$Q(2_1^+)$	0.59	0.12	
$Q(2_2^+)$	-1.22	-0.46	
$\mu(2_1^+)$	0.52	0.55	

^a Based on the mixing ratio $\delta = -0.35 \pm 0.02$.

^b Based on the mixing ratio $\delta = 11.0_{-0.5}^{+0.7}$.

^c Based on the mixing ratio $\delta = -0.36 \pm 0.02$.

^d Based on the mixing ratio $\delta = 16.0 \pm 2$.

^e Based on the mixing ratio $\delta = -0.25 \pm 0.5$.

^f Based on the mixing ratio $\delta = 4.4 \pm 0.3$.

ACKNOWLEDGMENTS

This work has been supported by JSPS KAKENHI Grant No. JP25K07293.

-
- [1] P. Federman and S. Pittel, *Phys. Lett. B* **69**, 385 (1977).
- [2] K. Heyde, P. Van Isacker, R. F. Casten, and J. L. Wood, *Phys. Lett. B* **155**, 303 (1985).
- [3] K. Heyde, C. De Coster, J. Jolie, and J. L. Wood, *Phys. Rev. C* **46**, 541 (1992).
- [4] J. L. Wood, K. Heyde, W. Nazarewicz, M. Huyse, and P. van Duppen, *Phys. Rep.* **215**, 101 (1992).
- [5] K. Heyde, J. Jolie, H. Lehmann, C. De Coster, and J. Wood, *Nucl. Phys. A* **586**, 1 (1995).
- [6] K. Heyde and J. L. Wood, *Rev. Mod. Phys.* **83**, 1467 (2011).
- [7] P. E. Garrett, M. Zielińska, and E. Clément, *Prog. Part. Nucl. Phys.* **124**, 103931 (2022).
- [8] S. Leoni, B. Fornal, A. Bracco, Y. Tsunoda, and T. Otsuka, *Prog. Part. Nucl. Phys.* **139**, 104119 (2024).
- [9] A. N. Andreyev, M. Huyse, P. Van Duppen, L. Weissman, D. Ackermann, J. Gerl, F. P. Hessberger, S. Hofmann, A. Kleinböhl, G. Münzenberg, S. Reshitko, C. Schlegel, H. Schaffner, P. Cagarda, M. Matos, S. Saro, A. Keenan, C. Moore, C. D. O’Leary, R. D. Page, M. Taylor, H. Kettunen, M. Leino, A. Lavrentiev, R. Wyss, and K. Heyde, *Nature (London)* **405**, 430 (2000).
- [10] J. Ojala, J. Pakarinen, P. Papadakis, J. Sorri, M. Sandzelius, D. M. Cox, K. Auranen, H. Badran, P. J. Davies, T. Grahn, P. T. Greenlees, J. Henderson, A. Herzán, R.-D. Herzberg, J. Hilton, U. Jakobsson, D. G. Jenkins, D. T. Joss, R. Julin, S. Juutinen, T. Kibédi, J. Konki, G. J. Lane, M. Leino, J. Limatainen, C. G. McPeake, O. Neuvonen, R. D. Page, E. Parr, J. Partanen, P. Peura, P. Rahkila, J. Revill, P. Ruotsalainen, J. Sarén, C. Scholey, S. Stolze, J. Uusitalo, A. Ward, and R. Wadsworth, *Communications Physics* **5**, 213 (2022).
- [11] R. Bengtsson, T. Bengtsson, J. Dudek, G. Leander, W. Nazarewicz, and J. ye Zhang, *Phys. Lett. B* **183**, 1 (1987).
- [12] R. Bengtsson and W. Nazarewicz, *Z. Phys. A* **334**, 269 (1989).
- [13] S. Cwiok, P. H. Heenen, and W. Nazarewicz, *Nature* **433**, 705 (2005).
- [14] P. E. Garrett, T. R. Rodríguez, A. D. Varela, K. L. Green, J. Bangay, A. Finlay, R. A. E. Austin, G. C. Ball, D. S. Bandyopadhyay, V. Bildstein, S. Colosimo, D. S. Cross, G. A. Demand, P. Finlay, A. B. Garnsworthy, G. F. Grinyer, G. Hackman, B. Jigmeddorj, J. Jolie, W. D. Kulp, K. G. Leach, A. C. Morton, J. N. Orce, C. J. Pearson, A. A. Phillips, A. J. Radich, E. T. Rand, M. A. Schumaker, C. E. Svensson, C. Sumithrarachchi, S. Triambak, N. Warr, J. Wong, J. L. Wood, and S. W. Yates, *Phys. Rev. Lett.* **123**, 142502 (2019).
- [15] P. E. Garrett, T. R. Rodríguez, A. Diaz Varela, K. L. Green, J. Bangay, A. Finlay, R. A. E. Austin, G. C. Ball, D. S. Bandyopadhyay, V. Bildstein, S. Colosimo, D. S. Cross, G. A. Demand, P. Finlay, A. B. Garnsworthy, G. F. Grinyer, G. Hackman, B. Jigmeddorj, J. Jolie, W. D. Kulp, K. G. Leach, A. C. Morton, J. N. Orce, C. J. Pearson, A. A. Phillips, A. J. Radich, E. T. Rand, M. A. Schumaker, C. E. Svensson, C. Sumithrarachchi, S. Triambak, N. Warr, J. Wong, J. L. Wood, and S. W. Yates, *Phys. Rev. C* **101**, 044302 (2020).
- [16] M. Spieker, P. Petkov, E. Litvinova, C. Müller-Gatermann, S. G. Pickstone, S. Prill, P. Scholz, and A. Zilges, *Phys. Rev. C* **97**, 054319 (2018).
- [17] C. M. Petrache, J.-M. Régis, C. Andreoiu, M. Spieker, C. Michelagnoli, P. E. Garrett, A. Astier, E. Dupont, F. Garcia, S. Guo, G. Häfner, J. Jolie, F. Kandzia, V. Karayonchev, Y.-H. Kim, L. Knafla, U. Köster, B. F. Lv, N. Marginean, C. Mihai, P. Mutti, K. Ortner, C. Porzio, S. Prill, N. Saed-Samii, W. Urban, J. R. Vanhoy, K. Whitmore, J. Wisniewski, and S. W. Yates, *Phys. Rev. C* **99**, 024303 (2019).
- [18] K. Ortner, C. Andreoiu, M. Spieker, G. C. Ball, N. Bernier, H. Bidaman, V. Bildstein, M. Bowry, D. S. Cross, M. R. Dunlop, R. Dunlop, F. H. Garcia, A. B. Garnsworthy, P. E. Garrett, J. Henderson, J. Measures, B. Olaizola, J. Park, C. M. Petrache, J. L. Pore, K. Raymond, J. K. Smith, D. Southall, C. E. Svensson, M. Ticu, J. Turko, K. Whitmore, and T. Zidar, *Phys. Rev. C* **102**, 024323 (2020).
- [19] J. Rikovska, N. Stone, P. Walker, and W. Walters, *Nucl. Phys. A* **505**, 145 (1989).
- [20] F. von Spee, M. Beckers, A. Blazhev, A. Dewald, F. Dunkel, A. Esmaylzadeh, C. Fransen, G. Hackenberg, J. Jolie, L. Knafla, C.-D. Lakenbrink, M. Schiffer, N. Warr, and M. Weinert, *Phys. Rev. C* **109**, 024325 (2024).
- [21] C. Mihai, A. A. Pasternak, S. Pascu, D. Filipescu, M. Ivaşcu, D. Bucurescu, G. C. ăta Danil, I. C. ăta Danil, D. Deleanu, D. G. Ghiţă, T. Glodariu, N. Mărginean, R. Mărginean, A. Negret, T. Sava, L. Stroe, G. Suliman, and N. V. Zamfir, *Phys. Rev. C* **83**, 054310 (2011).
- [22] E. A. Cederlöf, T. Bäck, J. Nyberg, C. Qi, A. Ataç, H. Badran, T. Braunroth, T. Calverley, D. M. Cox, M. Doncel, T. Grahn, P. Greenlees, J. Hilton, R. Julin, S. Juutinen, J. Konki, H. Li, S. Matta, V. Modamio, B. S. N. Singh, J. Pakarinen, P. Papadakis, J. Partanen, P. Rahkila, P. Ruotsalainen, M. Sandzelius, J. Sarén, C. Scholey, S. Stolze, P. Subramaniam, J. Uusitalo, and J. J. Valiente-Dobón, *Eur. Phys. J. A* **59**, 300 (2023).
- [23] C. B. Li, Y. Zheng, T. X. Li, X. G. Wu, H. Y. Wu, M. Zheng, Z. H. Zhao, Y. Q. Li, R. Hong, Z. Y. He, J. Z. Li, J. L. Wang, C. Y. Guo, Z. X. Zhou, L. Ni, G. S. Li, X. H. Zhou, B. Guo, S. Y. Wang, M. L. Liu, Y. H. Zhang, C. Y. He, F. L. Liu, S. Wang, and L. H. Zhu, *Phys. Rev. C* **109**, 034310 (2024).
- [24] S. Pascu, K. Kaneko, C. Qi, Y.-X. Liu, Y. Sun, N. Shimizu, T. Mizusaki, C. Mihai, M. Boromiza, D. Bucurescu, C. Costache, S. Călinescu, C. Clisu, A. Coman, I. Dinescu, D. Filipescu, N. M. Florea, I. Gheorghe, A. Ionescu, R. Lică, N. Mărginean, R. Mărginean, R. E. Mihai, A. Mitu, A. Negret, C. R. Niţă, C. Petrone, L. Stan, S. Toma, A. E. Turturică, G. Turturică, and S. Ujenuic, *Phys. Rev. C* **112**, 024312 (2025).
- [25] C. Qi, *Phys. Rev. C* **94**, 034310 (2016).
- [26] K. Kaneko, N. Shimizu, T. Mizusaki, and Y. Sun, *Phys. Rev. C* **103**, L021301 (2021).
- [27] S. Sharma, R. Devi, and S. K. Khosa, *Int. J. Mod. Phys. E* **31**, 2250053 (2022).
- [28] S. Sharma, R. Devi, and S. Khosa, *Nucl. Phys. A* **988**, 9 (2019).

- [29] D. Bonatsos, K. E. Karakatsanis, A. Martinou, T. J. Mertzimekis, and N. Minkov, *Phys. Rev. C* **106**, 044323 (2022).
- [30] L. Próchniak, K. Zajac, K. Pomorski, S. Rohoziński, and J. Srebrny, *Nucl. Phys. A* **648**, 181 (1999).
- [31] J. Libert, B. Roussière, and J. Sauvage, *Nucl. Phys. A* **786**, 47 (2007).
- [32] J. P. Delaroche, M. Girod, J. Libert, H. Goutte, S. Hilaire, S. Péru, N. Pillet, and G. F. Bertsch, *Phys. Rev. C* **81**, 014303 (2010).
- [33] http://www-phynu.cea.fr/science_en_ligne/carte_potentiels_microscopiques/carte_potentiel_nucleaire_eng.htm.
- [34] K. Suzuki and K. Nomura, *Phys. Rev. C* **110**, 064304 (2024).
- [35] M. Sambataro, *Nucl. Phys. A* **380**, 365 (1982).
- [36] H. Lehmann, J. Jolie, C. De Coster, B. Decroix, K. Heyde, and J. L. Wood, *Nucl. Phys. A* **621**, 767 (1997).
- [37] S. Pascu, N. V. Zamfir, G. C. ăta Danil, and N. Mărginean, *Phys. Rev. C* **81**, 054321 (2010).
- [38] J. B. Gupta, *Phys. Rev. C* **107**, 034315 (2023).
- [39] R. Budaca and A. I. Budaca, *Eur. Phys. J. Plus* **136**, 983 (2021).
- [40] E. A. Coello Pérez and T. Papenbrock, *Phys. Rev. C* **92**, 064309 (2015).
- [41] K. Heyde, P. Van Isacker, M. Waroquier, G. Wenes, and M. Sambataro, *Phys. Rev. C* **25**, 3160 (1982).
- [42] M. Délèze, S. Drissi, J. Kern, P. Tercier, J. Vorlet, J. Rikowska, T. Otsuka, S. Judge, and A. Williams, *Nucl. Phys. A* **551**, 269 (1993).
- [43] M. Délèze, S. Drissi, J. Jolie, J. Kern, and J. Vorlet, *Nucl. Phys. A* **554**, 1 (1993).
- [44] J. Jolie and H. Lehmann, *Phys. Lett. B* **342**, 1 (1995).
- [45] H. Lehmann and J. Jolie, *Nucl. Phys. A* **588**, 623 (1995).
- [46] C. De Coster, K. Heyde, B. Decroix, P. Van Isacker, J. Jolie, H. Lehmann, and J. L. Wood, *Nucl. Phys. A* **600**, 251 (1996).
- [47] P. E. Garrett, K. L. Green, H. Lehmann, J. Jolie, C. A. McGrath, M. Yeh, and S. W. Yates, *Phys. Rev. C* **75**, 054310 (2007).
- [48] P. E. Garrett, K. L. Green, and J. L. Wood, *Phys. Rev. C* **78**, 044307 (2008).
- [49] K. Nomura and J. Jolie, *Phys. Rev. C* **98**, 024303 (2018).
- [50] A. Leviatan, N. Gavrielov, J. E. García-Ramos, and P. Van Isacker, *Phys. Rev. C* **98**, 031302 (2018).
- [51] N. Gavrielov, J. E. García-Ramos, P. Van Isacker, and A. Leviatan, *Phys. Rev. C* **108**, L031305 (2023).
- [52] T. Otsuka, A. Arima, and F. Iachello, *Nucl. Phys. A* **309**, 1 (1978).
- [53] K. Nomura, R. Rodríguez-Guzmán, L. M. Robledo, and N. Shimizu, *Phys. Rev. C* **86**, 034322 (2012).
- [54] K. Nomura, T. Otsuka, and P. Van Isacker, *J. Phys. G: Nucl. Part. Phys.* **43**, 024008 (2016).
- [55] K. Nomura, R. Rodríguez-Guzmán, and L. M. Robledo, *Phys. Rev. C* **87**, 064313 (2013).
- [56] K. Nomura, R. Rodríguez-Guzmán, and L. M. Robledo, *Phys. Rev. C* **94**, 044314 (2016).
- [57] K. Nomura, R. Rodríguez-Guzmán, and L. M. Robledo, *Phys. Rev. C* **95**, 064310 (2017).
- [58] K. Nomura, R. Rodríguez-Guzmán, Y. M. Humadi, L. M. Robledo, and H. Abusara, *Phys. Rev. C* **96**, 034310 (2017).
- [59] D. Vretenar, A. V. Afanasjev, G. A. Lalazissis, and P. Ring, *Phys. Rep.* **409**, 101 (2005).
- [60] T. Nikšić, D. Vretenar, and P. Ring, *Prog. Part. Nucl. Phys.* **66**, 519 (2011).
- [61] T. Nikšić, N. Paar, D. Vretenar, and P. Ring, *Comput. Phys. Commun.* **185**, 1808 (2014).
- [62] A. Bjelčić, T. Nikšić, and Z. Drmač, DIRHBSpeedup, <https://github.com/abjelcic/DIRHBSpeedup.git> (2021).
- [63] A. Bohr and B. R. Mottelson, *Nuclear Structure*, Vol. II (Benjamin, New York, USA, 1975).
- [64] T. Nikšić, D. Vretenar, and P. Ring, *Phys. Rev. C* **78**, 034318 (2008).
- [65] Y. Tian, Z. Y. Ma, and P. Ring, *Phys. Lett. B* **676**, 44 (2009).
- [66] T. Otsuka, A. Arima, F. Iachello, and I. Talmi, *Phys. Lett. B* **76**, 139 (1978).
- [67] P. D. Duval and B. R. Barrett, *Phys. Lett. B* **100**, 223 (1981).
- [68] A. Frank, P. Van Isacker, and C. E. Vargas, *Phys. Rev. C* **69**, 034323 (2004).
- [69] K. Nomura, N. Shimizu, and T. Otsuka, *Phys. Rev. Lett.* **101**, 142501 (2008).
- [70] P. D. Duval and B. R. Barrett, *Nucl. Phys. A* **376**, 213 (1982).
- [71] Brookhaven National Nuclear Data Center, <http://www.nndc.bnl.gov>.
- [72] M. Doncel, T. Bäck, C. Qi, D. M. Cullen, D. Hodge, B. Cederwall, M. J. Taylor, M. Procter, M. Giles, K. Auranen, T. Grahn, P. T. Greenlees, U. Jakobsson, R. Julin, S. Juutinen, A. Herzán, J. Konki, J. Pakarinen, J. Partanen, P. Peura, P. Rakhila, P. Ruotsalainen, M. Sandzelius, J. Sarén, C. Scholey, J. Sorri, S. Stolze, and J. Uusitalo, *Phys. Rev. C* **96**, 051304 (2017).
- [73] F. Iachello and A. Arima, *The interacting boson model* (Cambridge University Press, Cambridge, 1987).
- [74] D. A. Testov, S. Bakes, J. J. Valiente-Dobón, A. Goasduff, S. Frauendorf, F. Nowacki, T. R. Rodríguez, G. de Angelis, D. Bazzacco, C. Boiano, A. Boso, B. Cederwall, M. Cicerchia, P. Čolović, G. Colucci, F. Didierjean, M. Doncel, J. A. Dueñas, F. Galtarossa, A. Gozzelino, K. Hadýnska-Klęk, G. Jaworski, P. R. John, S. Lenzi, H. Liu, S. Lunardi, R. Menegazzo, D. Mengoni, A. Mentana, D. R. Napoli, G. Pasqualato, F. Recchia, S. Riccetto, L. M. Robledo, M. Rocchini, B. Saygi, M. Siciliano, Y. Sobolev, and S. Szilner, *Phys. Rev. C* **103**, 044321 (2021).
- [75] M. Saxena, R. Kumar, A. Jhingan, S. Mandal, A. Stolarz, A. Banerjee, R. K. Bhowmik, S. Dutt, J. Kaur, V. Kumar, M. Modou Mbaye, V. R. Sharma, and H.-J. Wollersheim, *Phys. Rev. C* **90**, 024316 (2014).
- [76] B. Pritychenko, M. Birch, B. Singh, and M. Horoi, *At. Data Nucl. Data Tables* **107**, 1 (2016).
- [77] S. F. Hicks, G. K. Alexander, C. A. Aubin, M. C. Burns, C. J. Collard, M. M. Walbran, J. R. Vanhoy, E. Jensen, P. E. Garrett, M. Kadi, A. Martin, N. Warr, and S. W. Yates, *Phys. Rev. C* **71**, 034307 (2005).
- [78] S. F. Hicks, J. R. Vanhoy, P. G. Burkett, B. R. Champine, S. J. Etzkorn, P. E. Garrett, S. W. Yates, and M. Yeh, *Phys. Rev. C* **95**, 034322 (2017).
- [79] T. Grahn, S. Stolze, D. T. Joss, R. D. Page, B. Saygi, D. O'Donnell, M. Akmalı, K. Andgren, L. Bianco, D. M. Cullen, A. Dewald, P. T. Greenlees, K. Heyde, H. Iwasaki, U. Jakobsson, P. Jones, D. S. Judson,

- R. Julin, S. Juutinen, S. Ketelhut, M. Leino, N. Lumley, P. J. R. Mason, O. Möller, K. Nomura, M. Nyman, A. Petts, P. Peura, N. Pietralla, T. Pissulla, P. Rakhila, P. J. Sapple, J. Sarén, C. Scholey, J. Simpson, J. Sorri, P. D. Stevenson, J. Uusitalo, H. V. Watkins, and J. L. Wood, *Phys. Rev. C* **94**, 044327 (2016).
- [80] R. B. Cakirli, R. F. Casten, J. Jolie, and N. Warr, *Phys. Rev. C* **70**, 047302 (2004).
- [81] O. Möller, N. Warr, J. Jolie, A. Dewald, A. Fitzler, A. Linnemann, K. O. Zell, P. E. Garrett, and S. W. Yates, *Phys. Rev. C* **71**, 064324 (2005).
- [82] T. Wang, *Phys. Rev. C* **107**, 064303 (2023).
- [83] Y. Zhang and W. Teng, *Phys. Rev. C* **111**, 014324 (2025).
- [84] W. Teng, S. N. Wang, X. Z. Zhao, and Y. Zhang, *Nuclear Physics A* **1063**, 123214 (2025).
- [85] G. A. Lalazissis, T. Nikšić, D. Vretenar, and P. Ring, *Phys. Rev. C* **71**, 024312 (2005).
- [86] J. F. Berger, M. Girod, and D. Gogny, *Nucl. Phys. A* **428**, 23 (1984).
- [87] F. Wu, C. Andreoiu, V. Karayonchev, C. M. Petrache, J.-M. Régis, A. Esmaylzadeh, C. Michelagnoli, M. Beuschlein, P. Spagnoletti, G. Colombi, J. M. Daugas, L. Domenichetti, P. E. Garrett, J. Jolie, M. Ley, S. Pannu, and E. Taddei, *Phys. Rev. C* **111**, L051307 (2025).
- [88] P. Bonche, H. Flocard, and P. H. Heenen, *Compt. Phys. Commun.* **171**, 49 (2005).
- [89] W. Ryssens, V. Hellemans, M. Bender, and P.-H. Heenen, *Comput. Phys. Commun.* **187**, 175 (2015).
- [90] E. Chabanat, P. Bonche, P. Haensel, J. Meyer, and R. Schaeffer, *Nucl. Phys. A* **635**, 231 (1998).